

Draft : September 17, 2018

Radio Observations of the Hubble Deep Field South Region II: The 1.4 GHz Catalogue and Source Counts.

Minh T. Huynh¹

Research School of Astronomy & Astrophysics, The Australian National University, Mount Stromlo Observatory, Cotter Rd, Weston Creek, ACT 2611, Australia

`mhuynh@mso.anu.edu.au`

Carole A. Jackson

Australia Telescope National Facility, CSIRO Radiophysics Laboratory, PO Box 76, Epping, NSW 2121, Australia

Ray P. Norris

Australia Telescope National Facility, CSIRO Radiophysics Laboratory, PO Box 76, Epping, NSW 2121, Australia

Isabella Prandoni

Istituto di Radioastronomia, INAF, Via Gobetti 101, 40129, Bologna, Italy

ABSTRACT

This paper is part of a series describing the results from the *Australia Telescope Hubble Deep Field South* (ATHDFS) survey obtained with the *Australia Telescope Compact Array* (ATCA). This survey consists of observations at 1.4, 2.5, 5.2 and 8.7 GHz, all centred on the Hubble Deep Field South.

Here we present the first results from the extended observing campaign at 1.4 GHz. A total of 466 sources have been catalogued to a local sensitivity of 5σ (11 μ Jy rms). A source extraction technique is developed which: 1) successfully excludes spurious sources from the final source catalogues, and 2) accounts for the non-uniform noise in our image. A source catalogue is presented and the

¹affiliated with the Australia Telescope National Facility, CSIRO Radiophysics Laboratory, PO Box 76, Epping, NSW 2121, Australia

general properties of the 1.4 GHz image are discussed. We also present source counts derived from our ATHDFS 1.4 GHz catalogue. Particular attention is made to ensure the counts are corrected for survey incompleteness and systematic effects. Our counts are consistent with other surveys (e.g. ATESP, VIRMOS, and Phoenix Deep Field), and we find, in common with these surveys, that the HDFN counts are systematically lower.

Subject headings: catalogs — surveys — radio continuum: galaxies

1. Introduction

Early radio surveys found that classical radio galaxies ($S \gtrsim 1$ Jy) evolve strongly with time in both density and luminosity, and are relatively rare in the local universe (Longair 1966). More recent surveys which probe to fainter flux densities have shown that the normalised source count flattens below a few mJy (Windhorst et al. 1985). This flattening corresponds to a rapid increase in the number of faint radio sources, and has been interpreted as being due to a new population of sources which do not show up at higher flux density levels - the so called sub-mJy population. The existing sub-mJy samples are generally small due to the large amount of observing time required to reach these faint levels.

Several models, involving different classes of objects, have been developed to explain the observed sub-mJy source counts. These include a strongly evolving population of normal spiral galaxies (Condon 1984, 1989) or actively star forming galaxies (Windhorst 1984; Windhorst et al. 1985; Rowan-Robinson et al. 1993). A non evolving population of local ($z < 0.1$) low luminosity radio galaxies has also been proposed to explain the sub-mJy population (Wall et al. 1986). It is now thought that the sub-mJy population is comprised of low luminosity AGN, normal spirals and ellipticals, as well as starbursts, but the exact mix is unknown.

The nature of the sub-mJy population is still not clear because of the difficulty of obtaining optical photometry and spectra for complete radio samples. The follow up optical identification and spectroscopy of sub-mJy radio samples require a lot of telescope time because these sources generally have very faint optical counterparts. Conclusions about the sub-mJy sample have been inferred from surveys of varying radio sensitivity and different depths of optical follow up.

Approximately 41% of sub-mJy ($S_{1.4\text{GHz}} > 0.2$ mJy) radio sources are identified with optical counterparts to $m_B \sim 23.7$ and these are mostly faint blue galaxies with optical-infrared colours indicative of active star formation (Windhorst et al. 1985). This result is

confirmed by a spectroscopic study of optical counterparts ($B < 22$) to faint ($S_{1.4\text{GHz}} > 0.1\text{mJy}$) radio sources, which found that most of the sub-mJy sources have spectra similar to star forming *IRAS* galaxies (Benn et al. 1993). However, this result is obtained from spectroscopy of only 10% of their whole radio sample.

A more spectroscopically complete sample is the Marano field, where spectra were obtained for 50% of the 68 faint ($S_{1.4\text{GHz}} > 0.2\text{ mJy}$) radio sources (Gruppioni et al. 1999). Contrary to previous results of Benn et al. (1993), the majority of the spectra are identified with early type galaxies. Gruppioni et al. attribute this discrepancy to the fainter magnitude limit reached in their spectroscopic identifications, since the fraction of radio sources identified with early type galaxies increases abruptly at $B \sim 22.5$, which is the limit of the Benn et al. sample.

About 60% (219/386) of the faint ($S_{1.4\text{GHz}} > 0.5\text{ mJy}$) radio sources in the Australia Telescope ESO Slice Project (ATESP, Prandoni et al. 2000a) are identified to $I = 22.5$ mag. The spectra obtained for 70 sources with $I < 19$ are dominated by early type galaxies (60%). Starbursts and post-starburst galaxies become important in the sub-mJy ($S_{1.4\text{GHz}} < 1\text{ mJy}$) regime, where they make up 39% of the $I < 19$ sample (Prandoni et al. 2001b). Nevertheless, Prandoni et al. find that early type galaxies still constitute a significant fraction (25%) of the sub-mJy radio sources, and sub-mJy samples with fainter spectroscopic limits become increasingly sensitive to early type galaxies.

The Phoenix Deep Field survey covers a 4.5 deg^2 at 1.4 GHz and has a rms noise of $12\ \mu\text{Jy}$ over the most sensitive region (Hopkins et al. 2003). A subregion covering about a degree has been imaged to $R \sim 24.5$ and optical counterparts found for 76% of radio sources within the imaged area (Sullivan et al. 2004). Spectra of the radio sources revealed that the sub-mJy population is made up of at least 32% starforming galaxies and 21% are quiescent galaxies (Afonso et al. 2005). However, Afonso et al. (2005) only have spectra for 17% of their radio sources, and the spectral completeness is biased to the optically brighter radio sources ($R \lesssim 21$).

The most complete result in photometry is in the Hubble Deep Field North (HDFN) where the VLA was used to follow up observations of a patch of sky observed by the HST to depths of about 30th magnitude in the four HST broadband filters, F300W, F450W, F606W, and F814W (approximately U,B,V, and I). Eighty percent of the 79 faint ($S_{1.4\text{GHz}} \geq 0.04\text{ mJy}$) radio sources in the HDFN region were identified by HST and ground based images reaching $I_{\text{AB}} = 25$ (Richards et al. 1998; Richards 2000). Using optical and radio morphologies along with radio spectral index arguments, Richards et al. concluded that 60% of the HDFN radio sources with optical counterparts were star forming galaxies, 20% were classed as AGN, and the remainder were ambiguous.

In 1998, the HST observed a region of sky in the Southern continuous viewing zone (CVZ) as a complementary observation to the northern Hubble Deep Field (Williams et al. 1996). This field is known as the Hubble Deep Field South (HDFS) (Williams et al. 2000). A region containing a quasar suitable for the search of Lyman alpha absorption systems was chosen. The main WFPC field of the HDFS observations reach a magnitude limit of ~ 30 th magnitude in the four HST broadband filters. Simultaneous observations with the other HST instruments, NICMOS and STIS, reach similarly deep levels in the near-infrared and ultraviolet. In addition to the main HST deep fields, a mosaic of nine flanking fields were imaged to shallower levels of ~ 25 th in I (F814W). From the ground, deep wide field images have been obtained, reaching depths of ~ 25 th magnitude in UBVRI in a 44×44 arcmin region centered on the HDFS (Teplitz et al. 2001). Spectroscopically, 194 galaxies in the main HDFS and Flanking Fields were targeted on the Very Large Telescope (VLT) and reliable redshifts obtained for 97 targets (Sawicki & Mallén-Ornelas 2003). In addition, optical spectroscopy is available for 225 bright ($R < 24$) sources in a 9×3 arcmin region containing the STIS and WFPC fields (Glazebrook, in preparation, but see <http://www.aao.gov.au/hdfs/Redshifts/>).

The HDFS was selected as a region for deep radio follow up to take advantage of the wealth of publicly available optical/near-infrared photometric and spectroscopic data. Observations over 1998 to 2001 were performed on the Australia Telescope Compact Array (ATCA) at all four available frequency bands. Approximately 100 hours observing at each band yielded images at 1.4, 2.5, 5.2, and 8.7 GHz with sensitivities of approximately 10 μ Jy rms. A detailed description of observations, catalogues and analysis of these Australia Telescope Hubble Deep Field South (ATHDFS) images is described in Norris et al. (2004, hereafter Paper I).

The radio source counts at the faintest flux density levels ($S_{1.4\text{GHz}} < 1$ mJy) are not well determined due to the small number of surveys reaching this sensitivity regime. The sensitivity of our radio survey allows us to determine the source counts down to ~ 0.05 mJy. Only the Phoenix Deep Field (Hopkins et al. 2003) and Hubble Deep Field North Richards (2000) reach similarly deep levels.

This paper describes the image analysis and source extraction technique of the full 1.4 GHz ATHDFS survey. This paper is organised as follows. In Section 2 we summarise the 1.4 GHz observations and data reduction. Various image properties are discussed in Section 3 and the source extraction and catalogue is detailed in Section 4. Section 5 contains an analysis of the accuracy of our source parameters. The survey completeness is investigated in Section 6 and the ATHDFS 1.4 GHz differential radio source count is presented in Section 7.

2. Observations and Data Reduction

Paper I discussed in detail the observations and data reduction steps used to obtain the ATHDFS images. Here we provide a brief summary.

The 1.4 GHz observations were carried out over four years from 1998 to 2001. They consist of single pointings centred on RA = 22h 33m 25.96s and Dec = $-60^{\circ} 38' 09.0''$ (J2000). A wide variety of ATCA configurations was employed to ensure maximum uv coverage. The correlator was set to continuum mode (2×128 MHz bandwidth), with each 128 MHz bandwidth divided into 32×4 MHz channels. The primary flux density calibrator used was PKS B1934-638, while secondary gain and phase calibrations were performed through observations of either PKS B2205-636 or PKS B2333-528.

The data were inspected using the *MIRIAD* interactive task *TVFLAG*. After flagging, the 1.4 GHz data were split into the three observing bands (1.344, 1.384 and 1.432 GHz) before imaging and cleaning. This allowed the cleaning process to do a much better job of removing all the flux of a source. Two iterations of both phase and amplitude self-calibration were then performed to improve the image quality.

3. Image Analysis

In this Section we discuss two systematic effects which have to be taken into account in deriving source flux densities, the clean bias and bandwidth smearing. We use methods similar to those outlined in Prandoni et al. (2000b) to investigate clean bias and bandwidth smearing. A master equation to derive flux densities corrected for these effects is given in Appendix A.

3.1. Clean Bias

When the uv coverage is incomplete the cleaning process can redistribute flux from real sources to noise peaks, producing spurious sources. This effect is generally only a problem for snapshot observations where uv coverage is poor. Although our uv coverage is very good, tests were performed to check the magnitude of the clean bias in our image.

We performed a clean bias check by injecting point sources into the uv data at random positions. The uv data were then cleaned to the same rms level as our original image, and source peak fluxes after cleaning were compared to input values. The flux density distribution of injected sources was chosen to be similar to that of the real sources in the image : 40 at

5 σ , 15 at 6 σ , 15 at 7 σ , 15 at 8 σ , 15 at 9 σ , 10 at 10 σ , 3 at 20 σ , 2 at 30 σ , 1 at 50 σ and 1 at 100 σ . This simulation was repeated 50 times to get reliable number statistics.

The results from this process are shown in Figure 1. The average source flux measured after the cleaning process (S_{output}) normalised to the true source flux (S_{input}) is shown for the various values of input source signal-to-noise ($S_{\text{input}}/\sigma_{\text{local}}$). It is evident that clean bias only affects the faintest sources. There is a sudden increase in the clean bias at a flux density of about 10 σ , but even at the faintest bin (5 σ) the clean bias is only 4%.

An analytical form of the clean bias effect was obtained by a least squares fit to the function

$$S_{\text{output}}/S_{\text{input}} = a + b \frac{1}{S_{\text{input}}/\sigma_{\text{local}}}.$$

The best fit values for a and b are 1.00 and -0.23 , respectively. The resulting best fit curve is plotted in Figure 1.

3.2. Bandwidth Smearing

Bandwidth smearing, the radio analogue of optical chromatic aberration, is a well-known effect caused by the finite width of the receiver channels. It reduces the peak flux density of a source, while correspondingly increasing the source size in the radial direction such that the total integrated flux density is conserved. The amount of smearing is proportional to the distance from the phase centre, and the bandwidth of the observations. In the simplest case of a Gaussian beam and passband, the bandwidth smearing can be described by (Condon et al. 1998):

$$\frac{S_{\text{peak}}}{S_{\text{peak}}^O} \approx \frac{1}{\sqrt{1 + \frac{2 \ln 2}{3} \left(\frac{\Delta\nu}{\nu} \frac{d}{\theta_b} \right)^2}} \quad (1)$$

where the ratio $\frac{S_{\text{peak}}}{S_{\text{peak}}^O}$ represents the attenuation of the source peak flux density with respect to that of an unsmearred source, $\Delta\nu$ is the passband width, ν is the observing frequency, d is the distance from the phase centre, and θ_b is the synthesized beam FWHM.

Although the observational bandwidth is 4 MHz, the *MIRIAD* task *ATL0D* effectively doubles the channel bandwidth. So with the ATHDFS channel width ($\Delta\nu$) of 8 MHz and observing frequency (ν) of 1.4 GHz, Equation 1 simplifies to :

$$\frac{S_{\text{peak}}}{S_{\text{peak}}^O} \approx \frac{1}{\sqrt{1 + \frac{2 \ln 2}{91875} \left(\frac{d}{\theta_b} \right)^2}}. \quad (2)$$

The bandwidth smearing as a function of distance from the centre is plotted in Figure 2, calculated with the appropriate ATHDFS beamsize parameter. The majority of our radio sources lie within the inner 10×10 arcmin region, where the bandwidth smearing is less than 5%. The attenuation increases rapidly however, and is $\sim 18\%$ at a radial distance of 20 arcmin from the phase centre.

4. Source Extraction

4.1. The Noise Map

To investigate the noise characteristics of our 1.4 GHz image we constructed a noise map. The noise map which contains the pixel by pixel root mean square (rms) noise distribution was made using the SExtractor package (Bertin & Arnouts 1996). SExtractor initially estimates the local background in each mesh from the pixel data, and the local background histogram is clipped iteratively until convergence at $\pm 3\sigma$ around its median. The choice of mesh size is very important. When it is too small the background will be overestimated due to the presence of real sources. When it is too large, any small scale variations of the background are washed out.

We ran SExtractor with a mesh size set to 30×30 pixels, approximately 8×8 beams. A grey scale image of the SExtractor noise map is shown in Figure 3. As expected, the noise is lowest in the centre and increases with radial distance. The left panel of Figure 4 shows the average noise as a function of distance from the centre. This increase in noise is roughly a parabolic shape due to the primary beam attenuation. A histogram of the noise map pixel values is shown in the right panel of Figure 4. This distribution peaks at a value of $10 \mu\text{Jy}$, but has a large wing at high noise values ($\gtrsim 15 \mu\text{Jy}$) due to the radially increasing noise.

There are also regions of increased noise (white pixels) around bright sources which are clearly evident in the grey scale image (Figure 3). The increased noise around these sources is due to dynamic range effects, as discussed in Paper I. The most affected region is noticeable as a high noise bump at approximately 6 arcmin from the image centre in the left panel of Figure 4. This corresponds to the area surrounding the brightest source ($S_{1.4\text{GHz}} = 155 \text{ mJy}$). The noise in this region is up to 3 times that of the surrounding unaffected region.

Although SExtractor was developed for the analysis of optical data, the noise image obtained with it has been found to be reliable for radio images (Bondi et al. 2003). We confirmed the accuracy of the SExtractor noise map by comparing pixel values against rms values directly measured from our radio image. The directly measured values were obtained

by selecting a set of random positions in the 1.4 GHz image and calculating the rms in the surrounding 30×30 pixel box. Each box was examined for any sources above $3\sigma_{\text{local}}$ before inclusion in the analysis to ensure that flux from real sources does not effect the statistics. Figure 5 shows the mean and standard deviation of the difference between the SExtractor pixel values and the directly measured values as a function of distance from the centre. The difference is very close to zero, and there is no systematic effect as a function of radial distance. We therefore concluded that the SExtractor noise map is reliable and used it to perform the source extraction.

4.2. Source Detection and Fitting

We determined a sensible maximum radial distance for the source cataloging taking into account the following factors :

- i) the radial noise distribution,
- ii) the primary beam attenuation, and
- iii) the bandwidth smearing effect.

These three factors determine the efficacy of detecting a source with a particular flux density at different radial distances from the centre. The primary beam response at a radial distance of 20 arcmin is approximately 39%, resulting in an increased noise of $\sim 20 \mu\text{Jy}$, compared to $\sim 10 \mu\text{Jy}$ at the image centre. Furthermore, the bandwidth smearing effect is 18% at this distance and rapidly degrading, as discussed in Section 3.2. On this basis we choose to catalogue to a maximum distance of 20 arcmin from the image centre.

To begin the source extraction we divided the original 1.4 GHz map by the noise map generated by SExtractor, obtaining a ‘signal-to-noise’ map. SExtractor is useful for obtaining signal-to-noise maps, but it has not been reliably used for extracting sources from radio images. The commonly used routines are SFIND (Hopkins et al. 2002) and *IMSAD*. Although SFIND may result in fewer false detections (Hopkins et al. 2002), there are no systematic differences in the source parameters found by either routine (Schinnerer et al. 2004). We used the *MIRIAD* task *IMSAD* to derive a preliminary list of source ‘islands’. This task searches for ‘islands’ of pixels above a specified cutoff, and attempts to fit gaussian components to the ‘islands’. We executed *IMSAD* on the ‘signal-to-noise’ map to detect all islands with a peak flux density level of 4σ . This resulted in a list of 688 source ‘islands’ for further investigation.

Each source ‘island’ found by *IMSAD* was examined and refitted with an elliptical Gaussian to derive source flux densities and sizes. This refitting procedure was performed on the ‘real’ image (not the ‘signal-to-noise’ map). All sources and fit parameters were

visually inspected to check for obvious failures and poor fits that need further analysis. Following Prandoni et al. (2000b), a reference peak value was derived from a second degree interpolation of the source (*MIRIAD* task *MAXFIT*). If the difference between the fitted peak and reference peak was less than 20% of the reference value and the fitted position was inside the $0.9S_{\text{peak}}$ flux density contour, then these sources were assigned a fit quality flag of 1. Gaussian integrated fluxes were also compared to the ones directly measured by summing the pixels greater than 3σ in the source area. In most cases the Gaussian fit provided good values for the position and peak flux densities but not integrated flux densities. These sources are given a quality flag of 2 in the catalogue.

There were some problematic cases which were classified as follows :

- 1) sources fit by *IMSAD* with a single Gaussian, but better described by two or more Gaussians ($\sim 3\%$), and
- 2) non Gaussian sources not well fitted by a single Gaussian, i.e. fit exceeds tolerance criteria described above ($\sim 0.3\%$), and
- 3) obviously spurious sources which correspond to artefacts or noise peaks ($\sim 1\%$).

In the first case above, the *IMSAD* islands were split into two or three Gaussian components. The number of successfully split islands are 19 in total (18 with two components, 1 with three components). The individual components of these sources are listed in the catalogue.

The reference positions and peak flux densities from *MAXFIT* were adopted for the two non Gaussian sources. The source position angle was determined by the direction along which it is most extended. The FWHM size of the axes was defined by the distance between two points on the 3σ contour parallel to (major) and perpendicular to (minor) this direction. These sources are flagged “n” in the catalogue.

After accounting for the multiple components, non-Gaussian sources and noise artefacts, we have a list of 693 sources, or source components. Figure 6 shows the peak flux density and signal-to-noise distributions of the 4σ sample. The spurious sources were low SN, and make up about 4% of the $4 - 5\sigma$ sources. So to ensure we have a source catalogue of high reliability we apply a cut of 5σ , which includes 12 multiple component sources. There are clear signs of physical association between the individual components of these sources, as shown by the postage stamps in Figure 7. The final 5σ catalogue has 466 sources.

4.3. Deconvolution

The ratio of integrated flux to peak flux is a direct measure of the extension of a radio source:

$$S_{int}/S_{peak} = \frac{\theta_{maj}\theta_{min}}{b_{maj}b_{min}}, \quad (3)$$

where θ_{maj} and θ_{min} are FWHM of the source axes, and b_{maj} and b_{min} the FWHM of the synthesised beam axes. We therefore use this relation to determine whether our sources are resolved or unresolved (see e.g. Prandoni et al. 2000b; Bondi et al. 2003).

In Figure 8 we plot the ratio of the total integrated flux density (S_{int}) and peak flux density (S_{peak}) as a function of signal-to-noise (S_{peak}/σ) for all the sources in the catalogue. If the values of $S_{int} < S_{peak}$ are purely due to errors introduced by noise in our image, we can derive a criterion for extension by assuming that these statistical errors are also present for $S_{int} > S_{peak}$ sources. We determined the lower envelope in Figure 8 which contains 90% of the sources $S_{int} < S_{peak}$ and mirrored it above the $S_{int} = S_{peak}$ line. The upper envelope is characterised by the equation :

$$S_{int}/S_{peak} = 1 + \left[\frac{100}{(S_{peak}/\sigma)^3} \right]. \quad (4)$$

Only sources lying above this upper envelope and successfully deconvolved by *MIRIAD* are considered resolved. From this analysis we conclude that 221/466 (47%) of sources are resolved. Deconvolved sizes are only given in the catalogue for resolved sources, and other sources have deconvolved sizes set to zero.

4.4. Multiple Component Sources

Radio sources can be made up of a nucleus with hot spots along, and at the end of, one or two jets. The individual components of a single source are often catalogued separately by Gaussian fitting routines. This will skew number statistics, so a method must be devised to identify multiple components as belonging to a single source.

Similar to the technique of Magliocchetti et al. (1998), we plot the sum of the fluxes of the components of each nearest neighbour pair versus their separation, as shown in Figure 9. The high density of points to the bottom right of the θ -flux density plane is made up of the general population of single component sources. The pairs with a separation of about 10 arcsec are most likely subcomponents of single sources. This is evident from Figure 9 where the sources which were successfully split into multiple components in Section 4.2, shown as circled large dots, cluster around this separation.

We apply a maximum separation that increases with the summed flux density, S_{total} :

$$\theta = 100 \left(\frac{S_{\text{total}}(\text{mJy})}{10} \right)^{0.5} \text{ arcsec} . \quad (5)$$

This maximum separation is shown as a dashed line in Figure 9. By varying the allowed separation with summed flux, bright components may be considered a single source even at large separations, while faint sources are kept as single sources.

As a further constraint we apply a flux ratio cut to the nearest neighbour pairs. Since the flux densities of real double sources are correlated this gives us another criterion to restrict the matched pairs to physically associated sources. We combine pairs only if their flux densities differ by a factor less than 4. The sources which meet this further requirement are marked in Figure 9 by a large dot. For sources which lie to the left of Equation 5, 20/23 pairs with separations less than 20 arcsec pass the flux ratio cut, while only 3/21 pairs with larger separations are passed. So this procedure seems to be successful in that almost all pairs with small separation are considered single sources, while very few distant pairs are passed.

From this analysis we identify an additional 11 possible multiple sources. All of these sources were visually inspected and only 5 pairs appear to be real double sources with lobe-lobe or core-lobe morphology. The postage stamps of these pairs are shown in Figure 10. These sources are accepted as double sources and flagged in the catalogue. The other 6 pairs are shown in Figure 11. They are rejected as double sources as they show no sign of physical association.

4.5. The Catalogue

The full 5σ catalogue is presented in Table 1. A description of Table 1 is as follows.

Column (1) — Source ID.

Column (2) — Source name.

Column (3) — Right Ascension in J2000.

Column (4) — One sigma uncertainty of Right Ascension, in arcsec. This is calculated following Condon (1997) and Prandoni et al. (2000b).

Column (5) — Declination in J2000.

Column (6) — One sigma uncertainty of Declination, in arcsec. This is calculated following Condon (1997) and Prandoni et al. (2000b).

Column (7) — Source 1.4 GHz peak flux density, in mJy. The values given here are not corrected for the systematic effects described in Section 3 Appendix A describes how to obtain source peak flux densities corrected for the systematic effects.

Column (8) — Source 1.4 GHz integrated flux density, in mJy.

Column (9) and (10) — The *deconvolved* major and minor axes (FWHM) of the source, Θ , in arcsec. Zero values refer to unresolved sources (see Section 4.3).

Column (11) — The *deconvolved* position angle (PA, measured from N through E) of the source, in degrees. Zero values refer to unresolved sources (see Section 4.3).

Column (12) — The signal-to-noise ratio of the detection, calculated as *IMSAD* fitted peak/ σ_{local} .

Column (13) — Gaussian fit quality flag : “1” refers to very good fits, “2” refers to poor integrated flux density, and “n” refers to non-Gaussian sources. See Section 4.2 for more details.

Column (14) — Notes on associated sources : components of a multiple source are indicated with the name of the other source(s) with which they are associated. See Section 4.4 for more details.

5. Accuracy of Source Parameters

5.1. Internal Accuracy

We performed Monte Carlo simulations to check the internal accuracy of our Gaussian fits to the ATHDFS radio sources. Firstly, a residual map was produced by removing all the sources detected above 5σ . Gaussian sources were injected into the residual image at random positions and the *MIRIAD* Gaussian fitting task *IMFIT* was used to extract fitted parameters. The injected point sources had peak flux densities between 5σ and 100σ . Fifty sources were injected at each peak flux density level per simulation (500 in total), and the simulation was repeated 20 times to get a sample size of 1000 sources per flux density level. By comparing the input to fitted output parameters we test the reliability of our source parameters, and obtain an estimate of the fit errors.

In Figure 12 the ratio of the fitted peak flux density (S_{output}) to input peak flux density (S_{input}) is shown as a function of the source signal-to-noise. There is an evident systematic effect (known as “noise bias”) in the fitted peak flux density for sources with signal-to-noise ratios less than about 10σ . Here the ratio of fitted to input peak flux density deviates

from unity due to incompleteness at the lower signal-to-noise bins. If an injected source is coincident with a noise dip, its peak flux density is either under-estimated or it falls below the source detection threshold. This biases the fitted flux density to higher values because only sources that fall on noise peaks, and therefore have extra flux, are detected and measured.

Figure 13 shows the ratio of output to input source sizes for both major and minor axes. There may be a marginal systematic over-estimation of the source major axis for sources with signal-to-noise less than about 20σ . Although the output major axis sizes are increasingly over-estimated from 20σ to 5σ , the over-estimation is less than the standard deviation in the measurements. In contrast there is no systematic effect present on the measurement of the minor axis.

The accuracy of source positions was also checked in the simulations. The mean difference between output and input positions ($\Delta\alpha$ and $\Delta\delta$) are plotted in Figure 14 as a function of source signal-to-noise. No systematics are present, and we notice that rms values for the two axes (α and δ) are similar. The positional accuracy of our catalogue is therefore derived as 1.1 arcsec at the limit of our survey (5σ), improving to 0.6 arcsec at 10σ and 0.1 arcsec at 100σ .

5.2. Absolute Accuracy

Ideally, our survey would be checked against an independent radio survey to determine the absolute accuracy of the source parameters. Unfortunately there are no radio surveys in the region which reach the required depth. The Parkes-MIT-NRAO (PMN) survey (Griffith & Wright 1993) has a flux density limit of only 30 mJy at 4.85 GHz, while the Sydney University Molonglo Sky Survey (SUMSS, Mauch et al. 2003) reaches a peak flux density limit of 6 mJy at 843 MHz. The SUMSS source positions are not useful as a comparison because the SUMSS resolution is about 45 arcsec and source positional uncertainties are up to 10 arcsec, which are much greater than the ATHDFS internal positional uncertainties. Flux density comparisons are not possible since these two surveys are at different frequencies and there is no a priori knowledge of the source SEDs.

The absolute positional accuracy of our survey will depend on how well the positions of the phase calibrators are known. Calibrator PKS B2333-528 has been observed by VLBI and its position in the FK5 reference system is known to within 0.005 arcsec in each coordinate (Ma et al. 1998). The position of the second calibrator, PKS B2205-636, is known to within 0.1 – 0.25 arcsec (ATCA calibrator manual, <http://www.narrabri.atnf.csiro.au/calibrators/>). Thus we expect the absolute accuracy of our source positions to be 0.25 arcsec. This absolute

uncertainty in position is not included in the catalogue (Table 1), and needs to be added in quadrature to the source positional uncertainty. This affects mainly the brighter sources, as the positional uncertainty of sources with signal-to-noise less than 10 are dominated by the internal accuracy of our survey.

6. Survey Completeness

In the ATHDFS, sources were included in the catalogue if the measured peak flux density exceeded five times the local noise. This can lead to incompleteness at faint flux density levels, which has to be taken into account when deriving source counts. In this Section we discuss the various possible sources of incompleteness in the source catalogue.

6.1. Visibility Area

Any source extraction method that relies on the ratio of peak flux density to the local noise will be affected by the variation of noise in the image. The area over which a source of a given flux density can be detected, also known as the visibility area, depends on the source peak flux density and the homogeneity of the noise distribution. The noise in our image is $11.0 \mu\text{Jy}$ at the centre and is a function of the primary beam response, increasing towards the edges of the field, as quantified in Section 4.1. Local variation in image noise is also caused by bright sources, which can increase the noise in its vicinity by up to 3 times that of an unaffected region (see Section 4.1 for details).

The visibility area of the ATHDFS 1.4 GHz image is shown in Figure 15. As expected, the fraction of the total area over which a source of a given peak flux density can be detected increases between 0.05 and 0.1 mJy, and reaches 0.96 at 0.1 mJy. The rise in the visibility function is not as rapid as in the ATESP (Prandoni et al. 2001a) or VIRMOS (Bondi et al. 2003) surveys. This is because these surveys used a mosaicing technique, which results in a more uniform noise distribution than single-pointing surveys such as the ATHDFS. The visibility area also shows that sources with a peak flux density greater than 0.1 mJy can be detected over more than 95% of the whole image. The visibility area reaches 100% of the image at a peak flux density of 0.23 mJy.

6.2. Systematic Effects

Two additional effects which could be responsible for partial incompleteness in the source catalogue are bandwidth smearing and clean bias. These two effects have been extensively discussed in Section 3. Bandwidth smearing can lead to an underestimation of peak flux densities by up to $\sim 18\%$, although the amount is 5% or less for the majority of our sources. The clean bias affects both peak and integrated flux densities. It leads to an underestimation of flux densities by $\sim 5\%$ for the faintest sources ($5\sigma_{\text{local}}$), but has no effect on sources brighter than $10\sigma_{\text{local}}$.

In Section 3 we proposed a formula (Equation A1) to correct the measured peak and integrated flux densities for these two systematic effects. The correction depends on the source signal-to-noise ratio as well as the source distance from the image centre. However, peak flux densities are underestimated by $\sim 23\%$ *at most* due to the combined effects of both clean bias and bandwidth smearing. Since the highest level of noise is $\sim 50 \mu\text{Jy}$, it follows that clean bias and bandwidth smearing do not affect sources brighter than $5 \times 50 \mu\text{Jy} / 0.77 \sim 0.32 \text{ mJy}$.

6.3. Resolution Bias

Resolution bias is an effect in which weak extended sources may have peak flux densities that fall below the catalogued 5σ limit, yet still have total integrated flux densities above the survey limit. To derive a source count that is complete in terms of total flux density, the number of “missing” sources has to be estimated. Given a maximum detectable angular size and knowledge of the intrinsic source size distribution as a function of flux density, this so called resolution bias can be corrected. Here we follow the procedures of Prandoni et al. (2001a) to correct the resolution bias.

Assuming a Gaussian beam, the maximum size (θ_{max}) a source of total flux density S_{total} can have before it drops below the $5\sigma_{\text{local}}$ detection limit can be calculated from the equation:

$$\frac{S_{\text{total}}}{5\sigma_{\text{local}}} = \frac{\theta_{\text{max}}^2}{b_{\text{maj}}b_{\text{min}}}. \quad (6)$$

In Figure 16 we plot the angular size (θ) of the ATHDFS sources as a function of the measured total flux density. The angular sizes are defined as the geometric mean of the major and minor deconvolved axes of the sources. We assume $S_{\text{total}} = S_{\text{peak}}$ for point sources. We calculate θ_{max} from Equation 6 with a full range of noise values from 5 to 30 μJy . The distribution of pixel values in the noise image of Section 4.1 is used to determine the relative

weight of each noise value and a weighted average θ_{\max} is calculated. Figure 16 shows that the angular sizes of the largest ATHDFS sources are in good agreement with this weighted average θ_{\max} function.

As discussed in 4.3, the deconvolution efficiency depends on the signal-to-noise of a source. An estimate of the minimum angular size (θ_{\min}) that a source can have is derived from Equations 3 and 4:

$$\frac{S_{\text{total}}}{S_{\text{peak}}} = 1 + \left[\frac{100}{(S_{\text{total}}/\sigma_{\text{local}})^3} \right] = \frac{\theta_{\min}^2}{b_{\text{maj}}b_{\text{min}}} \quad (7)$$

Similar to the derivation of θ_{\max} , a weighted average θ_{\min} is calculated using the noise distribution of our image. The resulting average θ_{\min} is plotted in Figure 16 as a dashed line. We note that the θ_{\min} constraint is important at low flux density levels where θ_{\max} becomes unphysical ($\rightarrow 0$). Also, the minimum deconvolved size is about $10''$ at the detection limit, whereas sources as small as $\sim 1''$ are reliably deconvolved at higher signal-to-noise.

Using the two constraints described above, an overall angular size upper limit, θ_{lim} , as a function of flux density S_{total} is defined as:

$$\theta_{\text{lim}} = \max(\theta_{\max}, \theta_{\min}) \quad (8)$$

The incompleteness of the ATHDFS survey due to θ_{lim} can be estimated with knowledge of the true source angular size distribution as a function of flux density. We assume an exponential form for the integral angular size distribution, $h(\theta)$ (Windhorst et al. 1990):

$$h(\theta) = e^{-\ln 2(\theta/\theta_{\text{med}})^{0.62}} \quad (9)$$

with

$$\theta_{\text{med}} = 2'' S_{1.4\text{GHz}}^{0.30}, \quad (10)$$

where $S_{1.4\text{GHz}}$ is in mJy, and θ_{med} is the estimated median source size at a given flux density. Equations 9 and 10 together with Equation 8 allow us to estimate the fraction of sources larger than the maximum detectable size and therefore missed by our survey. The correction factor, c , is then simply calculated as:

$$c = \frac{1}{1 - h(\theta)}. \quad (11)$$

In Figure 17 we show both $h(\theta)$ (left panel) and c (right panel). The resolution bias peaks at about 0.1 mJy, but decreases at lower flux densities due to the θ_{\min} constraint.

7. The ATHDFS 1.4 GHz Source Counts

In this Section, we construct the differential radio source counts from the 5σ ATHDFS catalogue. In computing the source counts we have used the integrated flux density for resolved sources and peak flux densities for point sources. The counts were calculated by dividing the number of sources in each flux density bin by the total survey area and the bin width, and then normalising by the Euclidean slope of $S^{-2.5}$. The reason for the normalisation is historical, relating to the early use of radio source counts to test various cosmological models against the number of sources that would be expected in a steady state Euclidean universe (Longair 1966; Ryle 1968).

Table 2 lists the final ATHDFS source counts, corrected for the visibility area, clean bias, bandwidth smearing and resolution bias as discussed above. For each flux density bin, the mean flux density ($\langle S \rangle$), the number of detected sources (N), the number of effective sources after applying the corrections (N_{eff}), and the corrected normalised differential radio source count (dN/dS), are given. We show the counts before and after corrections in Figure 18. We notice that the corrections are most important in the flux density range 0.09 – 0.3 mJy, where they can increase the source count by up to approximately 30%.

Sources classed as "multiple-component" (see Section 4.4) only make one contribution to the source count. At these flux density levels, the difference between incorporating "multiple-component" sources as single objects and deriving counts from the "full component" catalogue is negligible. If all components are used, then the most significant change is in the $\langle S \rangle = 0.119$ mJy bin, where there are 4 additional sources. For this bin the difference is $\sim 7\%$, which is less than the Poisson error.

7.1. Comparison To Other Deep Radio Source Counts

The ATHDFS source counts are compared to those derived from other 1.4 GHz surveys in Figure 19. The source counts from the Faint Images of the Radio Sky at Twenty centimetres survey (FIRST, White et al. 1997) are shown, as well as counts from the ATESP survey (Prandoni et al. 2001a), Phoenix Deep Field (PDF, Hopkins et al. 2003) and Hubble Deep Field North (HDFN, Richards 2000). The solid line in Figure 19 is the linear least squares sixth order polynomial fit to this compilation of source counts. FIRST counts below 2.5 mJy, were removed from the fit since FIRST is incomplete at this limit. PDF counts above 2.5 mJy and ATESP counts above 76 mJy were also excluded from the fit since the sampling is sparse in the higher flux density bins of these surveys. The resulting polynomial fit is given

by:

$$\log[(dN/dS)/(S^{-2.5})] = \sum_{i=0}^6 a_i (\log[S/\text{mJy}])^i, \quad (12)$$

with $a_0 = 0.841$, $a_1 = 0.540$, $a_2 = 0.364$, $a_3 = -0.063$, $a_4 = -0.107$, $a_5 = 0.052$ and $a_6 = -0.007$. For comparison, a third order fit to source counts from 0.1 mJy to 10000 mJy by (Katgert et al. 1988) and a sixth order fit by (Hopkins et al. 2003) to the PDF and FIRST source counts between 0.06 mJy and 1 mJy are shown as dashed and dotted lines, respectively. A third order polynomial is insufficient to account for the curvature below 0.1 mJy suggested by both the HDFN and PDF surveys. A fourth order polynomial does not adequately model the point of inflection around 0.5 mJy (Hopkins et al. 2003), while fifth order polynomials do not reproduce the concave curvature seen at about 1 Jy (e.g. Windhorst et al. 1990; Katgert et al. 1988). Hence the sixth order polynomial is necessary. The fitted polynomial has no physical basis, but is useful in quantifying the differential radio source count.

There is a high level of consistency between the source counts derived from both small and large area surveys at flux densities $S_{1.4\text{GHz}} > 0.5$ mJy (Figures 19 and 20). The differential source counts diverge at fainter flux density levels ($S_{1.4\text{GHz}} < 0.5$ mJy) The source count from the HDFN has been previously noted as being particularly low because of inadequate completeness corrections, as well as cosmic variance (Richards 2000; Hopkins et al. 2003). In contrast, the count from the ATHDFS lies *higher* than all other counts at $S_{1.4\text{GHz}} \sim 0.4$ mJy, although within statistical agreement for $S_{1.4\text{GHz}} < 0.3$ mJy. The excess is significant for the ATHDFS at $0.37 \text{ mJy} < S_{1.4\text{GHz}} < 0.47 \text{ mJy}$ compared to the latest (2003) PDF results and the counts from the VIRMOS survey. Over the 0.35 deg^2 area catalogued by the ATHDFS survey, we have 22 sources in this flux density range, compared to 44 in the VIRMOS field (1 deg^2) and 150 in the latest PDF catalogue (4.5 deg^2). We attribute the variation in the ATHDFS as real given the small area of the ATHDFS, with a probable over density of $\sim 3 - 8$ sources compared to the 'average' field.

At the very faintest limits ($S_{1.4\text{GHz}} < 0.1$ mJy) it has been suggested that the differential source count steepens towards lower flux density limits (Hopkins et al. 2003; Richards 2000). Although there is little real confirmation, as in every case it relies on the faintest source count bin, this steepening is expected as the 'flat' region of the count between 0.08 and 0.3 mJy cannot continue infinitely because the implied surface density of radio sources would exceed the number of host galaxies (Windhorst et al. 1993). The differential count from the ATHDFS is in agreement with the general trend around $S = 0.08$ mJy, although the last data point at 0.059 mJy lies well above those from the HDFN and PDF. Thus we cannot confirm the down-turn in the differential radio source count, and will have to wait for a deeper source catalogue to supply this data.

7.2. Source Counts and Galaxy Evolution

Source counts are important because they can be used to constrain the evolution of the radio population. The source count above 10 mJy is dominated by giant radio galaxies and QSOs, which we group together in this discussion as AGN. At sub-mJy levels (0.1 – 1 mJy) there is an increasing number of blue galaxies with starforming spectral signatures. Condon (1989), Rowan-Robinson et al. (1993), Hopkins et al. (1998) and others have concluded that the source count at these faintest levels requires two populations, AGN and starforming galaxies, both of which undergo strong evolution.

To derive a local luminosity function of starforming galaxies, Hopkins et al. (1998) start with the IRAS 60 μ m luminosity function (Saunders et al. 1990) and convert that to radio using the well-known FIR-radio correlation (Helou & Bica 1993; Yun et al. 2001). Assuming that luminosity evolves as $(1+z)^q$, Hopkins et al. (1998) found $q = 3.3 \pm 0.8$ best matches the radio source counts.

We perform a similar test to determine the rate of evolution of the local starforming galaxies required to match the radio source counts. We use the local radio luminosity function of starforming galaxies determined by Condon et al. (2002) for the 4583 Uppsala Galaxy Catalogue (UGC, Nilson 1973) galaxies crossmatched with the NRAO VLA Sky Survey (NVSS, Condon et al. 1998). The UGC-NVSS local RLF is the most comprehensive to date, very local ($z < 0.02$), and probes the low luminosity end of starforming galaxies to $\log(L_{1.4\text{GHz}}) = 18.8 \text{ W Hz}^{-1}$. The UGC-NVSS local RLF, $\rho_m(L)$, is described by the local visibility function, $\phi \equiv L^{5/2}\rho(L)$, where

$$\log(\phi) = \log[\rho_m(L)] + \frac{3}{2} \log[L] + 28.43 .$$

Fitting the visibility function directly, instead of the RLF, results in a better fit because the $L^{5/2}$ weighting prevents the visibility function from steepening as fast as the luminosity function at high luminosities. Condon et al. (2002) approximate the visibility function with a hyperbolic function:

$$\log(\phi) = Y - \left\{ B^2 + \left[\frac{\log(L) - X}{W} \right]^2 \right\}^{1/2} ,$$

with $Y = 3.06$, $B = 1.9$, $X = 22.35$, and $W = 0.67$, for starforming galaxies. For the AGN component we use the AGN counts from Jackson (2004).

The observed source count is shown in Figure 21 along with several models for the counts of the local starforming population. We have explored a variety of evolution scenarios: pure luminosity evolution going as $(1+z)^q$, pure density evolution going as $(1+z)^p$, and a

no evolution model. We confirm that two distinct populations, the starforming galaxies and AGN, are required to account for the faint source counts. The counts are best fit by starforming galaxies undergoing $(1+z)^{2.7}$ luminosity evolution. This amount of evolution means the number of starforming galaxies exceeds the number of AGN at about 0.25 mJy. The counts rule out stronger luminosity evolution of $q \gtrsim 4$. A modest amount of density evolution is also allowed, but if it is large (e.g. $p \gtrsim 6$) the source counts are too high at the μJy level. A downturn in radio source counts is needed at these levels so that the number of radio sources don't exceed the number of host galaxies (Windhorst et al. 1993). Thus, the radio source counts rule out large amounts of density evolution in the starforming galaxy population.

Similar values for the evolution of star forming galaxies have been found by Hopkins (2004) and Seymour et al. (2004), who find $q = 2.7$ and $q = 2.5$, respectively. These two studies use the local radio luminosity function of starforming galaxies from Sadler et al. (2002). Despite different assumptions for the luminosity functions of both starforming and AGN galaxies, there is good agreement between our work and these previous studies.

Redshift information is required to break the degeneracy between luminosity and density evolution. Little density evolution is expected however. For example, Hopkins (2004) jointly constrain the evolution parameters q and p to find $q = 2.7$ and $p = 0.15$. We have obtained spectra of our radio sources which will allow us to explore galaxy evolution in detail. This further work will be discussed in a future paper.

8. Summary

We have presented the extended observations of the Hubble Deep Field South with the Australia Telescope Compact Array at 1.4 GHz. The new 1.4 GHz image reaches a maximum sensitivity of $\sim 11 \mu\text{Jy}$ rms at a resolution of ~ 6.5 arcsec. The clean bias and bandwidth smearing effects have been investigated and quantified for our 1.4 GHz image. A catalogue of all sources brighter than $5\sigma_{\text{local}}$ within 20 arcmin of the image centre has been compiled, comprising 466 sources.

The 1.4 differential radio source counts from the ATHDFS survey have been presented. We have corrected the counts for survey completeness and systematic effects, including visibility area, clean bias, bandwidth smearing and resolution bias. We find that the source counts in the ATHDFS are in general consistent with that from previous surveys, although the ATHDFS counts are greater than that found in the the HDFN by a factor of 1.2 – 2. Other deep surveys have also found the HDFN counts to be low (e.g. Phoenix, Hopkins et al.

2003; VIRMOS, Bondi et al. 2003). Thus, the HDFN counts are probably underestimated, or the HDFN samples a relatively under-dense region of radio sources. We find the radio source counts are best fit by the local starforming population with luminosity evolution of the form $(1 + z)^{2.7}$, although small amounts of density evolution are not ruled out.

The ATHDFS survey has obtained radio images at 2.5, 5.2 and 8.7 GHz in addition to 1.4 GHz. The next paper in the series will provide radio spectral indices and a detailed analysis of the ATHDFS sources across this radio spectrum. The Hubble Deep Field South has also been the target of deep multi-colour optical photometry and spectroscopy. Future papers in this series will present the optical identifications and spectroscopy of the ATHDFS radio sources.

The authors thank the referee for helpful comments that improved this paper. MTH is grateful to have had support from an ANU PhD Stipend Scholarship and CSIRO-CNR bilateral travel funds. The Australia Telescope Compact Array is part of the Australia Telescope which is funded by the Commonwealth of Australia for operation as a National Facility managed by CSIRO.

A. Flux density corrections for systematic effects

As discussed in Section 3, the two systematics which affect the peak flux densities of the ATHDFS sources have been analysed. These two effects are the clean bias and bandwidth smearing. The flux densities given in the ATHDFS catalogue (Table 2) are not corrected for these effects. Corrected flux densities can be obtained using the following formula :

$$S_{\text{corr}} = \frac{S_{\text{meas}} \sqrt{1 + \frac{2 \ln 2}{91875} \left(\frac{d}{\theta_b}\right)^2}}{1.00 - 0.23(S_{\text{meas}}/\sigma)^{-1}}, \quad (\text{A1})$$

where S_{meas} is the flux density actually measured and catalogued, S_{meas}/σ is the catalogued source signal-to-noise, d is the source distance from the pointing centre (RA = 22h 33m 37.6s, Dec = $-60^\circ 33' 29''$), and θ_b is the synthesized beam FWHM (6.6"). The term in the numerator of Equation A1 corrects for the bandwidth smearing, while the term in the denominator represents the clean bias correction. For integrated flux densities, the term in the numerator of Equation A1 should be set to 1.

REFERENCES

Afonso, M., et al. 2005, submitted to ApJ

- Benn, C. R., Rowan-Robinson, M., McMahon, R. G., Broadhurst, T. J., & Lawrence, A. 1993, MNRAS, 263, 98
- Bertin, E., & Arnouts, S. 1996, A&AS, 117, 393
- Bondi, M., et al. 2003, A&A, 403, 857
- Condon, J. J. 1984, ApJ, 287, 461
- Condon, J. J. 1989, ApJ, 338, 13
- Condon, J. J. 1997, PASP, 109, 166
- Condon, J. J., Cotton, W. D., & Broderick, J. J. 2002, AJ, 124, 675
- Condon, J. J., Cotton, W. D., Greisen, E. W., Yin, Q. F., Perley, R. A., Taylor, G. B., & Broderick, J. J. 1998, AJ, 115, 1693
- Georgakakis, A., Mobasher, B., Cram, L., Hopkins, A., Lidman, C., & Rowan-Robinson, M. 1999, MNRAS, 306, 708
- Griffith, M. R., & Wright, A. E. 1993, AJ, 105, 1666
- Gruppioni, C., Mignoli, M., & Zamorani, G. 1999, MNRAS, 304, 199
- Helou, G., & Bica, M. D. 1993, ApJ, 415, 93
- Hopkins, A. M. 2004, ApJ, 615, 209
- Hopkins, A. M., Afonso, J., Chan, B., Cram, L. E., Georgakakis, A., & Mobasher, B. 2003, AJ, 125, 465
- Hopkins, A. M., Miller, C. J., Connolly, A. J., Genovese, C., Nichol, R. C., & Wasserman, L. 2002, AJ, 123, 1086
- Hopkins, A. M., Mobasher, B., Cram, L., & Rowan-Robinson, M. 1998, MNRAS, 296, 839
- Jackson, C. A. 2004, in Science with the Square Kilometre Array
- Katgert, P., Oort, M. J. A., & Windhorst, R. A. 1988, A&A, 195, 21
- Longair, M. S. 1966, MNRAS, 133, 421
- Ma, C., et al. 1998, AJ, 116, 516
- Magliocchetti, M., Maddox, S. J., Lahav, O., & Wall, J. V. 1998, MNRAS, 300, 257

- Mauch, T., Murphy, T., Buttery, H. J., Curran, J., Hunstead, R. W., Piestrzynski, B., Robertson, J. G., & Sadler, E. M. 2003, *MNRAS*, 342, 1117
- Nilson, P. 1973, *Uppsala general catalogue of galaxies (Acta Universitatis Upsaliensis. Nova Acta Regiae Societatis Scientiarum Upsaliensis - Uppsala Astronomiska Observatoriums Annaler, Uppsala: Astronomiska Observatorium, 1973)*
- Prandoni, I., Gregorini, L., Parma, P., de Ruiter, H. R., Vettolani, G., Wieringa, M. H., & Ekers, R. D. 2000a, *A&AS*, 146, 31
- Prandoni, I., Gregorini, L., Parma, P., de Ruiter, H. R., Vettolani, G., Wieringa, M. H., & Ekers, R. D. 2000b, *A&AS*, 146, 41
- Prandoni, I., Gregorini, L., Parma, P., de Ruiter, H. R., Vettolani, G., Wieringa, M. H., & Ekers, R. D. 2001a, *A&A*, 365, 392
- Prandoni, I., Gregorini, L., Parma, P., de Ruiter, H. R., Vettolani, G., Zanichelli, A., Wieringa, M. H., & Ekers, R. D. 2001b, *A&A*, 369, 787
- Richards, E. A. 2000, *ApJ*, 533, 611
- Richards, E. A., Kellermann, K. I., Fomalont, E. B., Windhorst, R. A., & Partridge, R. B. 1998, *AJ*, 116, 1039
- Rowan-Robinson, M., Benn, C. R., Lawrence, A., McMahon, R. G., & Broadhurst, T. J. 1993, *MNRAS*, 263, 123
- Ryle, M. 1968, *ARA&A*, 6, 249
- Sadler, E. M., Jackson, C. A., Cannon, R. D., McIntyre, V. J., Murphy, T., Bland-Hawthorn, J., Bridges, T., Cole, S., Colless, M., Collins, C., Couch, W., Dalton, G., De Propriis, R., Driver, S. P., Efstathiou, G., Ellis, R. S., Frenk, C. S., Glazebrook, K., Lahav, O., Lewis, I., Lumsden, S., Maddox, S., Madgwick, D., Norberg, P., Peacock, J. A., Peterson, B. A., Sutherland, W., & Taylor, K. 2002, *MNRAS*, 329, 227
- Saunders, W., Rowan-Robinson, M., Lawrence, A., Efstathiou, G., Kaiser, N., Ellis, R. S., & Frenk, C. S. 1990, *MNRAS*, 242, 318
- Sawicki, M., & Mallén-Ornelas, G. 2003, *AJ*, 126, 1208
- Schinnerer, E., Carilli, C. L., Scoville, N. Z., Bondi, M., Ciliegi, P., Vettolani, P., Le Fèvre, O., Koekemoer, A. M., Bertoldi, F., & Impey, C. D. 2004, *AJ*, 128, 1974
- Seymour, N., McHardy, I. M., & Gunn, K. F. 2004, *MNRAS*, 352, 131

- Sullivan, M., Hopkins, A. M., Afonso, J., Georgakakis, A., Chan, B., Cram, L. E., Mobasher, B., & Almeida, C. 2004, *ApJS*, 155, 1
- Teplitz, H. I., Hill, R. S., Malumuth, E. M., Collins, N. R., Gardner, J. P., Palunas, P., & Woodgate, B. E. 2001, *ApJ*, 548, 127
- Wall, J. V., Benn, C. R., Grueff, G., & Vigotti, M. 1986, *Highlights in Astronomy*, 7, 345
- White, R. L., Becker, R. H., Helfand, D. J., & Gregg, M. D. 1997, *ApJ*, 475, 479
- Williams, R. E., Baum, S., Bergeron, L. E., Bernstein, N., Blacker, B. S., Boyle, B. J., Brown, T. M., Carollo, C. M., Casertano, S., Covarrubias, R., de Mello, D. F., Dickinson, M. E., Espey, B. R., Ferguson, H. C., Fruchter, A., Gardner, J. P., Gonnella, A., Hayes, J., Hewett, P. C., Heyer, I., Hook, R., Irwin, M., Jones, D., Kaiser, M. E., Levay, Z., Lubenow, A., Lucas, R. A., Mack, J., MacKenty, J. W., Madau, P., Maki-don, R. B., Martin, C. L., Mazzuca, L., Mutchler, M., Norris, R. P., Perriello, B., Phillips, M. M., Postman, M., Royle, P., Sahu, K., Savaglio, S., Sherwin, A., Smith, T. E., Stiavelli, M., Suntzeff, N. B., Teplitz, H. I., van der Marel, R. P., Walker, A. R., Weymann, R. J., Wiggs, M. S., Williger, G. M., Wilson, J., Zacharias, N. & Zurek, D. R. 2000, *AJ*, 120, 2735
- Williams, R. E., Blacker, B., Dickinson, M., Dixon, W. V. D., Ferguson, H. C., Fruchter, A. S., Giavalisco, M., Gilliland, R. L., Heyer, I., Katsanis, R., Levay, Z., Lucas, R. A., McElroy, D. B., Petro, L., Postman, M., Adorf, H. & Hook, R. 1996, *AJ*, 112, 1335
- Windhorst, R., Mathis, D., & Neuschaefer, L. 1990, in *Evolution of the universe of galaxies; Proceedings of the Edwin Hubble Centennial Symposium*, Berkeley, CA, June 21-23, 1989 (A91-55951 24-90). San Francisco, CA, Astronomical Society of the Pacific, 1990, p. 389-403., 389
- Windhorst, R. A. 1984, *Faint radio galaxy populations. Deep radio surveys and multicolor photometry* (Leiden: Sterrewacht, 1984)
- Windhorst, R. A., Fomalont, E. B., Partridge, R. B., & Lowenthal, J. D. 1993, *ApJ*, 405, 498
- Windhorst, R. A., Miley, G. K., Owen, F. N., Kron, R. G., & Koo, D. C. 1985, *ApJ*, 289, 494
- Yun, M. S., Reddy, N. A., & Condon, J. J. 2001, *ApJ*, 554, 803

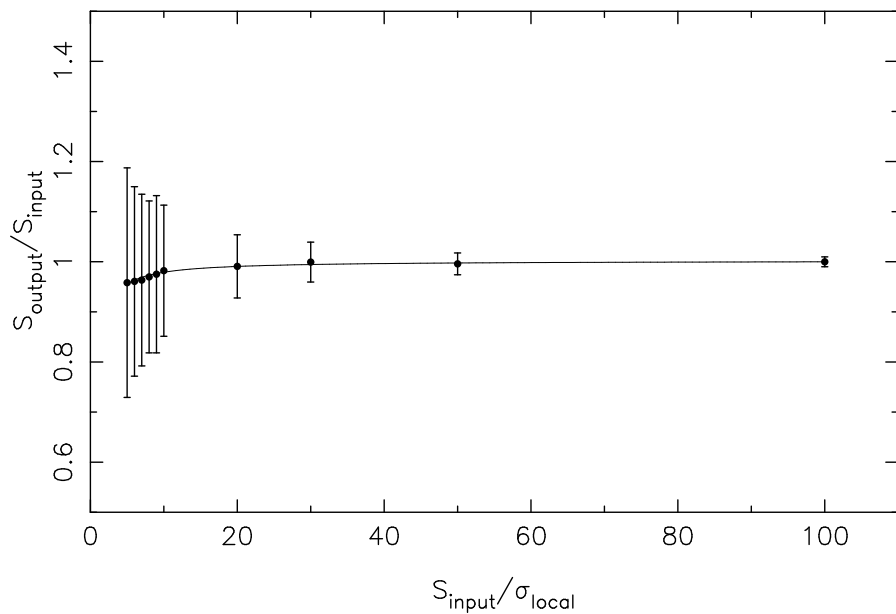


Fig. 1.— The source flux measured after the cleaning process (S_{output}) normalised to the true source flux (S_{input}), as a function of the input source signal-to-noise ($S_{\text{input}}/\sigma_{\text{local}}$). Also shown is the best fit curve (see Section 3.1), which is indistinguishable from the data.

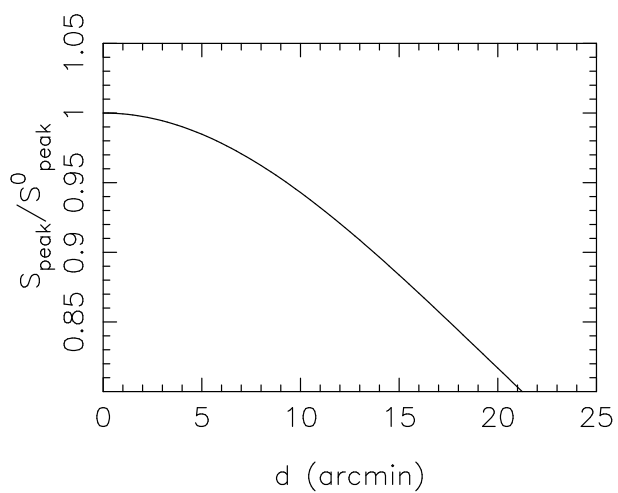


Fig. 2.— Bandwidth smearing effect, as a function of distance from the phase centre.

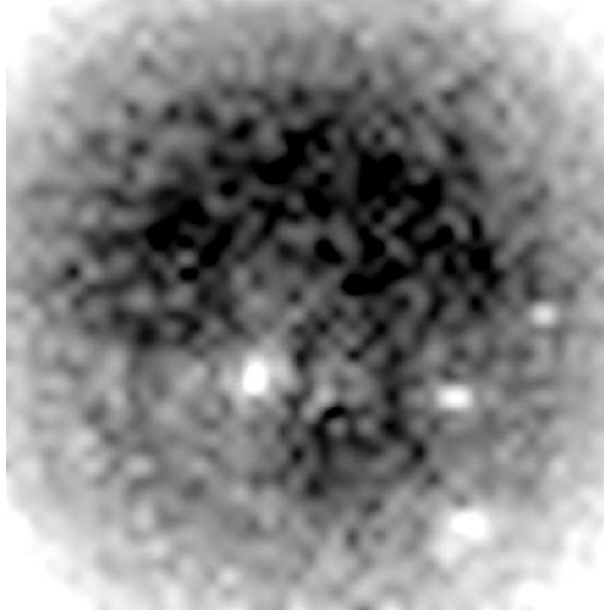


Fig. 3.— A grey scale of the noise map obtained by SExtractor. The image is 40×40 arcmin, and darker regions indicate lower noise.

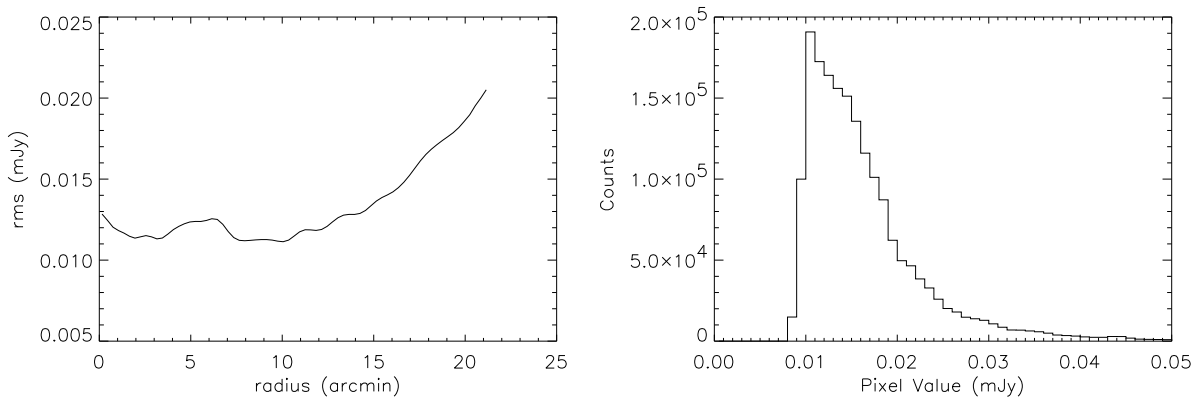


Fig. 4.— Left panel: Noise (radially averaged) as a function of radial distance for the SExtractor noise map. The broad peak around 5-7 arcmin is due to the noise region around the bright 155 mJy source (ATHDFS_J223355.6–604315). Right panel: Distribution of the pixel values of the SExtractor noise map.

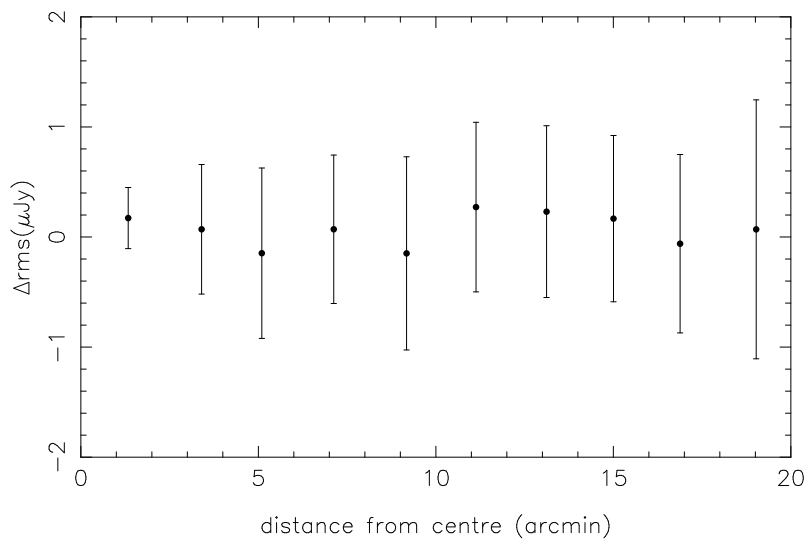


Fig. 5.— Mean difference between directly measured rms value and the corresponding value in the SExtractor noise map as a function of radial distance.

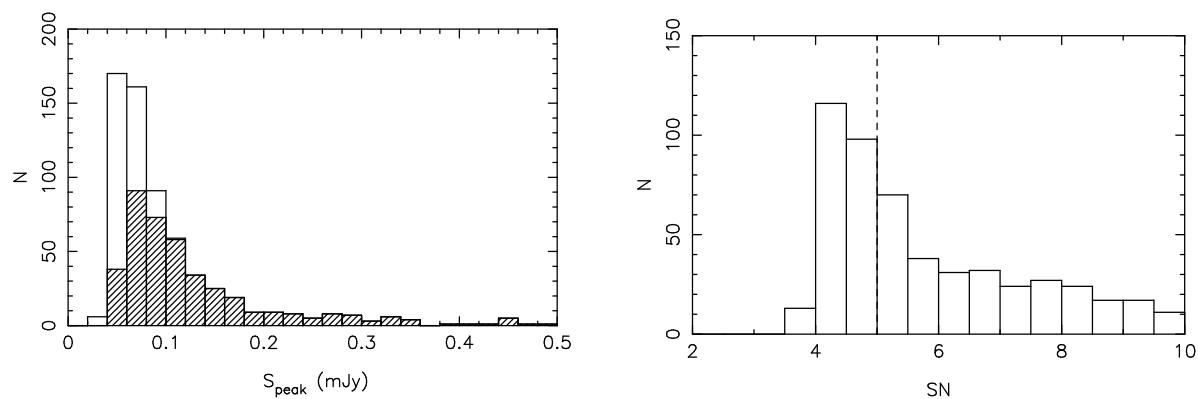


Fig. 6.— Peak flux density (left panel) and signal-to-noise (right panel) distribution of the 4σ ATHDFS sample, extracted as described in Section 4.2. The peak flux density distribution of the final 5σ catalogue is shown as the hatched region in the left panel. The catalogue 5σ cutoff is shown as a dashed line in the right panel.

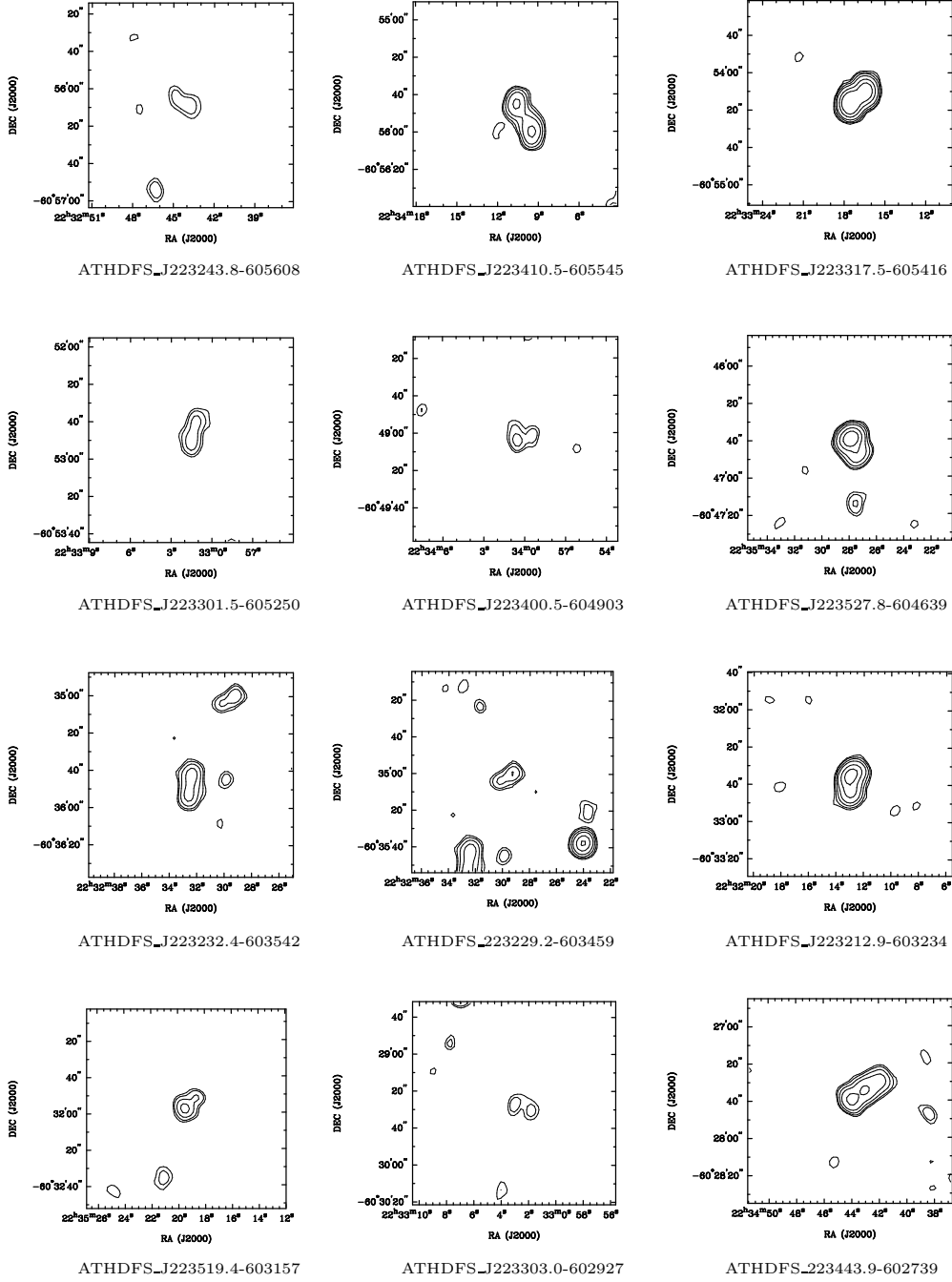


Fig. 7.— Postage stamps, $1.8' \times 1.8'$ in size, of the twelve 1.4 GHz sources fit by multiple Gaussians. The contour levels for each source are set at 3, 5, 10, 20, 50 and 100 σ .

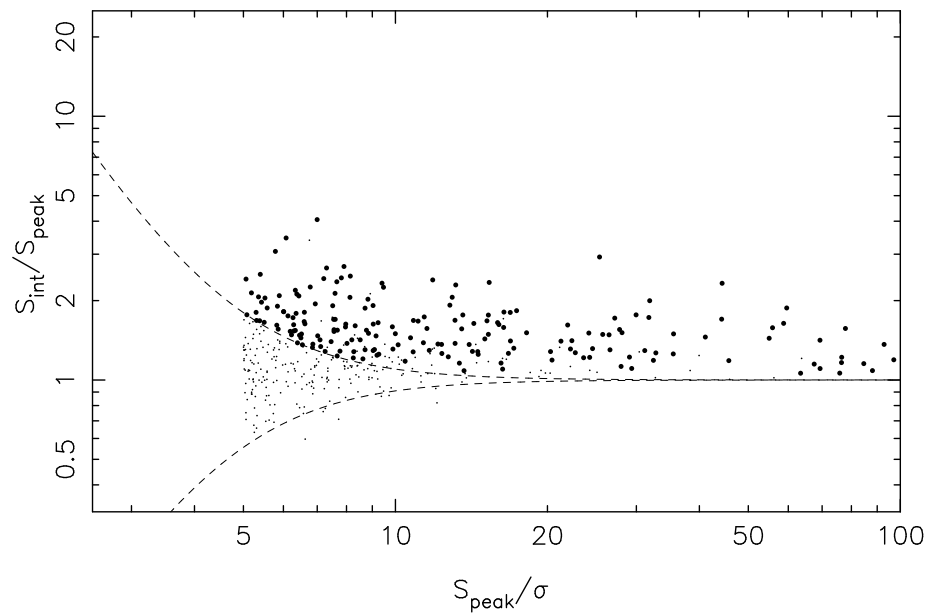


Fig. 8.— Ratio of the integrated flux density (S_{int}) to the peak flux density (S_{peak}) as a function of source signal-to-noise (S_{peak}/σ). The dashed lines show the upper and lower envelopes of the flux ratio distribution that contains 90% of the unresolved sources (*small dots*). The *large dots* indicate sources which are deconvolved successfully and considered resolved.

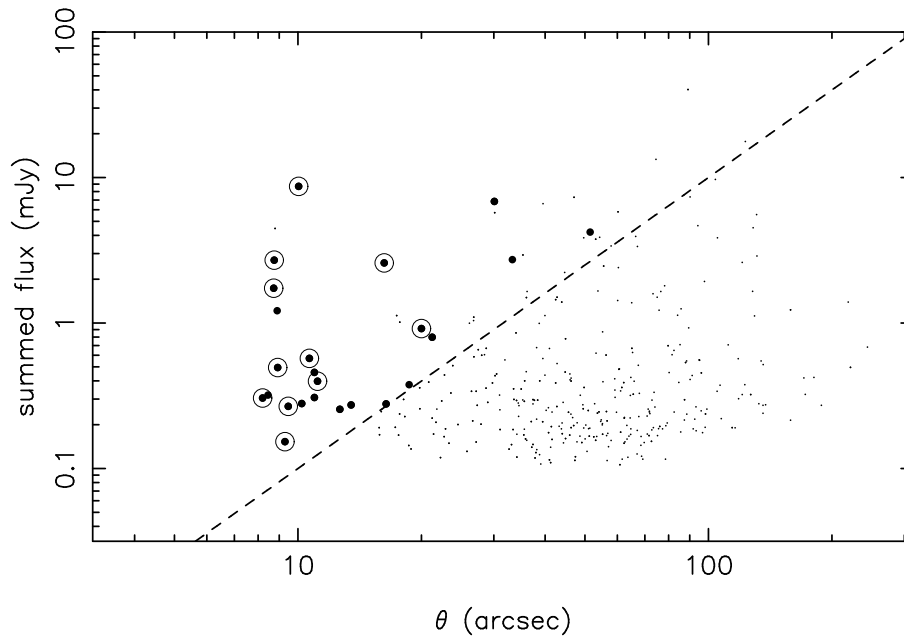


Fig. 9.— Sum of the flux densities of nearest neighbour pairs plotted against their separation. Source pairs which lie to the left of the line (see Section 4.4 for details) are considered as possible double sources. The source pairs with flux densities that differ by less than a factor of 4 are shown as *large dots*. As a comparison, all sources already well fit by 2 or more Gaussian components in Section 4.2 have been outlined with a *large circle*.

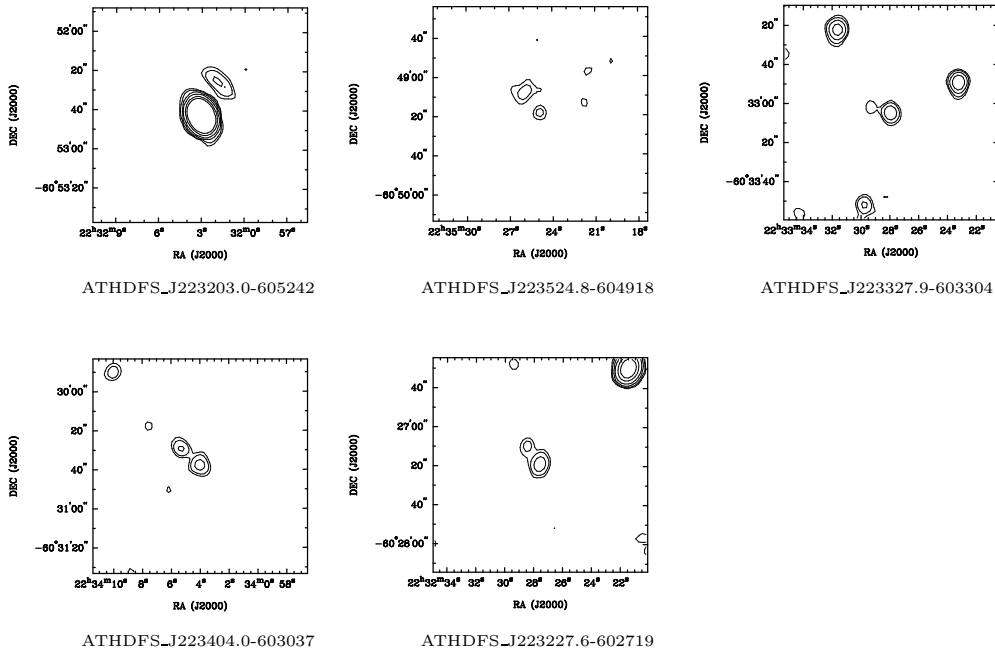


Fig. 10.— Postage stamps, $1.8' \times 1.8'$ in size, of the 5 source pairs which pass the single source test described in Section 4.4 and appear to be physically associated. The contour levels for each source are set at 3, 5, 10, 20, 50 and 100σ .

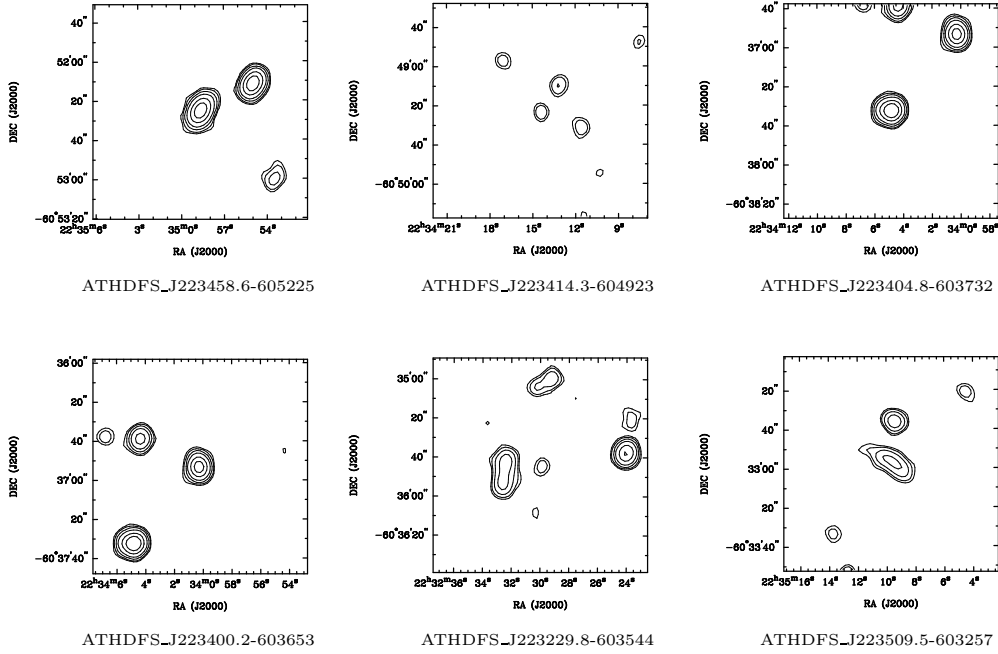


Fig. 11.— Postage stamps, $1.8' \times 1.8'$ in size, of the 6 source pairs which pass the single source test described in Section 4.4 but are not taken to be physically associated. The contour levels for each source are set at 3, 5, 10, 20, 50 and 100σ .

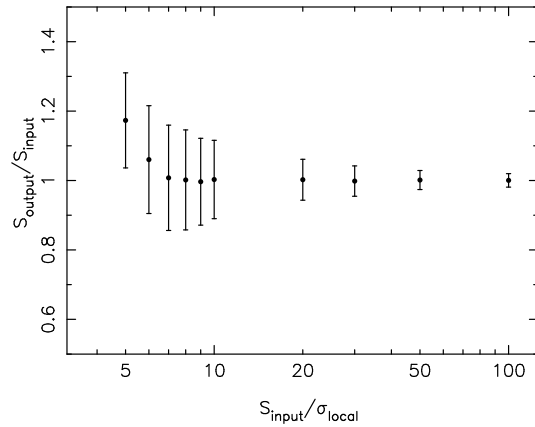


Fig. 12.— The mean and standard deviation of output/input peak flux densities for the injected sources, as a function of signal-to-noise.

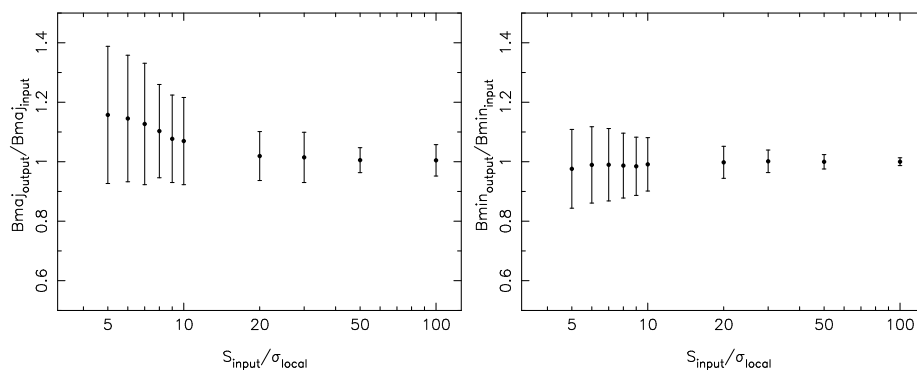


Fig. 13.— The mean and standard deviation of output/input axis FWHMs for the injected sources, as a function of signal-to-noise. Left panel : major axis. Right panel : minor axis.

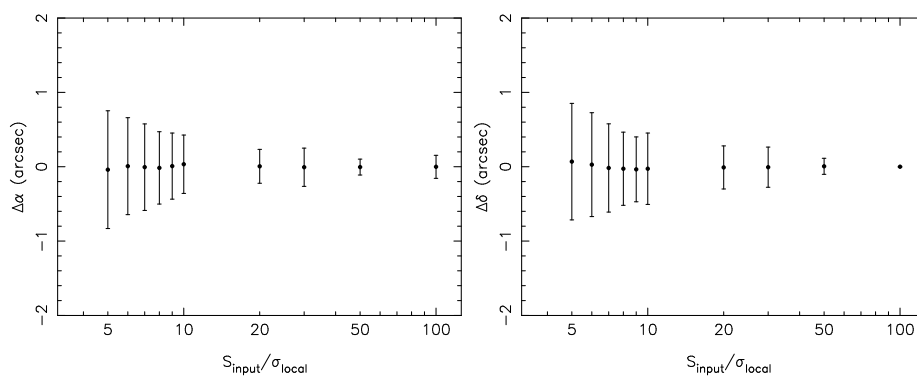


Fig. 14.— The mean and standard deviation for the difference in output position to input positions of injected sources, as a function of signal-to-noise. Left panel : right ascension. Right panel : declination.

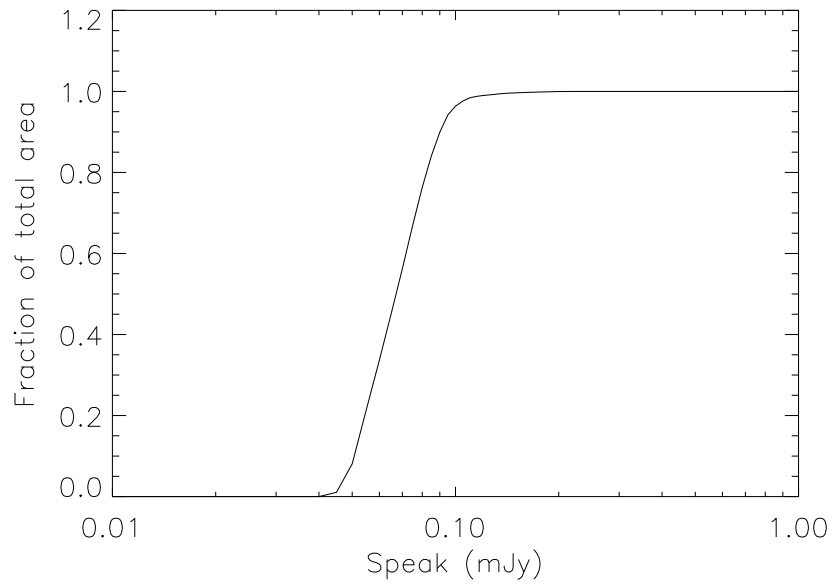


Fig. 15.— Visibility area of the single-pointing ATHDFS 1.4 GHz image. Fraction of the total area over which a source of measured peak flux density S_{peak} could be detected. The rise in visibility area is less steep than in Prandoni et al. (2001a) (c.f their Figure 1.)

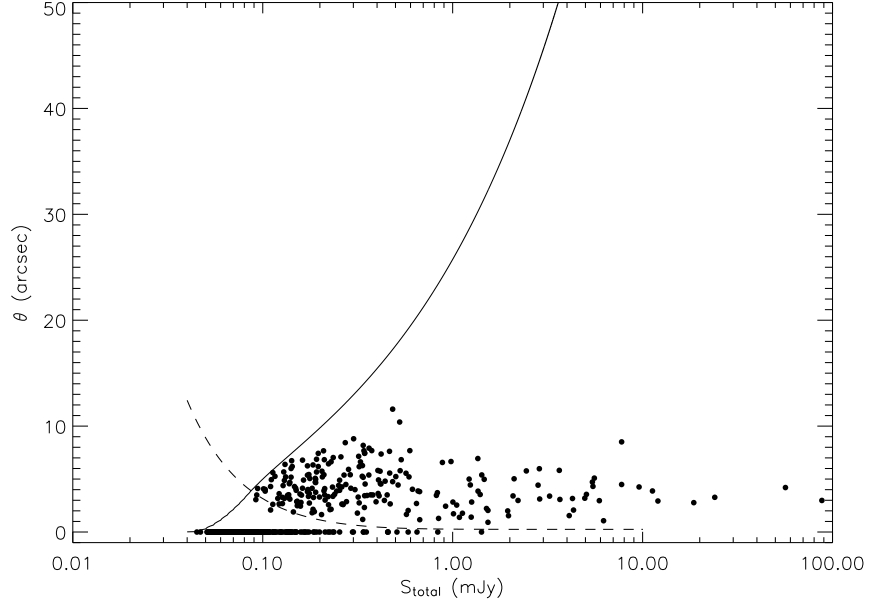


Fig. 16.— Angular size (geometric mean of deconvolved axes) for the ATHDFS sources as a function of the measured to flux density. Unresolved sources have deconvolved sizes, and therefore angular sizes, set to zero. The maximum size (θ_{max}) a source can have before dropping below the detection limit is shown as a solid line. Also drawn is the minimum angular size (θ_{min}) reliably deconvolved as a function of flux density (dashed line).

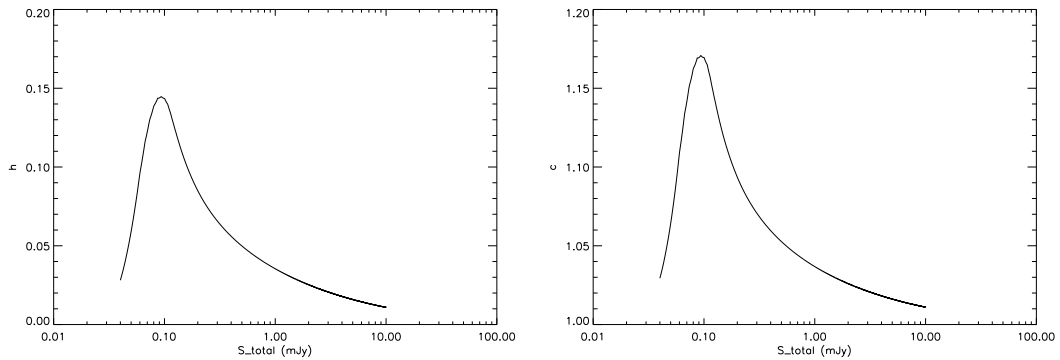


Fig. 17.— Left panel: Fraction of sources with angular sizes greater than θ_{lim} , $h(\theta_{\text{lim}})$, as a function of flux density. Right panel: The resolution bias correction, $c = \frac{1}{1-h(\theta_{\text{lim}})}$.

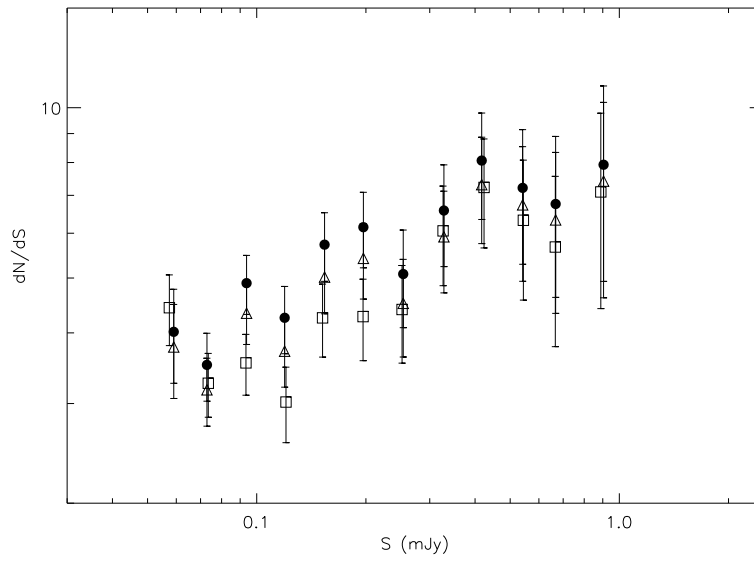


Fig. 18.— The 1.4 GHz normalised differential radio source counts derived from the ATHDFS catalogue. The source counts before correcting for clean bias, bandwidth smearing and resolution bias are shown as *squares*. *Triangles* indicate the counts after correcting for clean bias and bandwidth smearing, but not resolution bias. Source counts with full corrections are shown as *circles*.

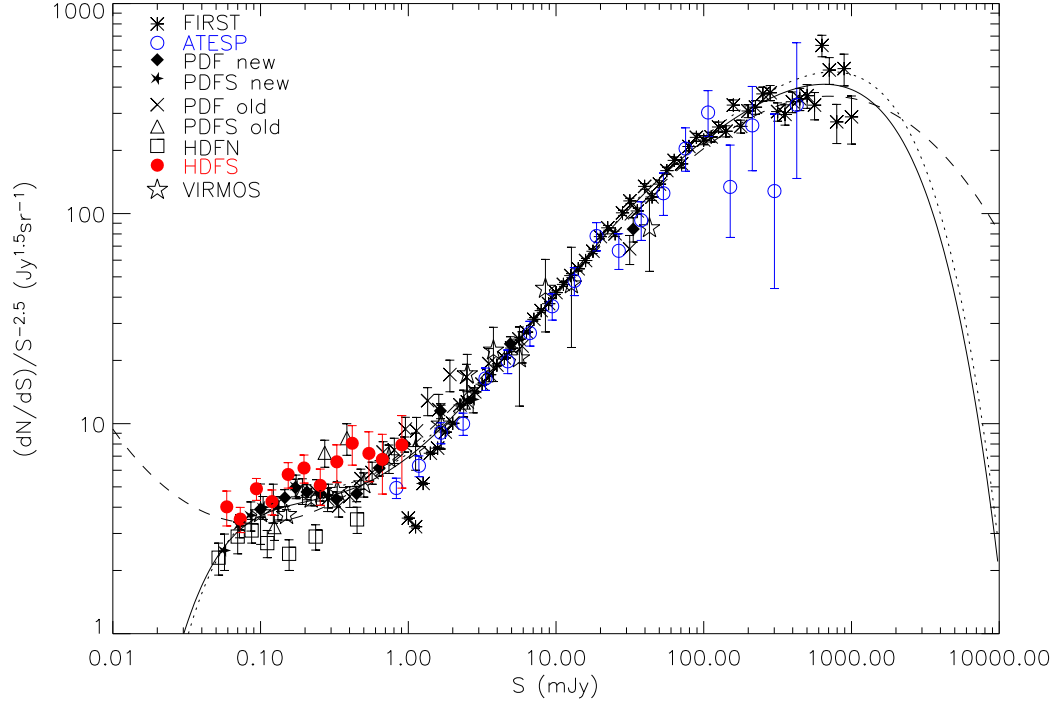


Fig. 19.— Normalised 1.4 GHz differential radio source counts: FIRST (*asterisks*; White et al. 1997), the original Phoenix Deep Field survey (*crosses* and *triangles*; Hopkins et al. 1998), the latest Phoenix Deep Field survey (*diamonds* and *filled stars*; Hopkins et al. 2003), the ATESP survey (*empty circles*; Prandoni et al. 2001a), the Hubble Deep Field North (*empty squares*; Richards 2000), the ATHDFS (*filled circles*), and the VIRMOS survey (*empty stars*; Bondi et al. 2003). The solid line is a sixth order polynomial fit described in the text. The sixth order fit from Hopkins et al. (2003) (dotted line) and third order fit from Katgert et al. (1988) (dashed line) are shown for comparison.

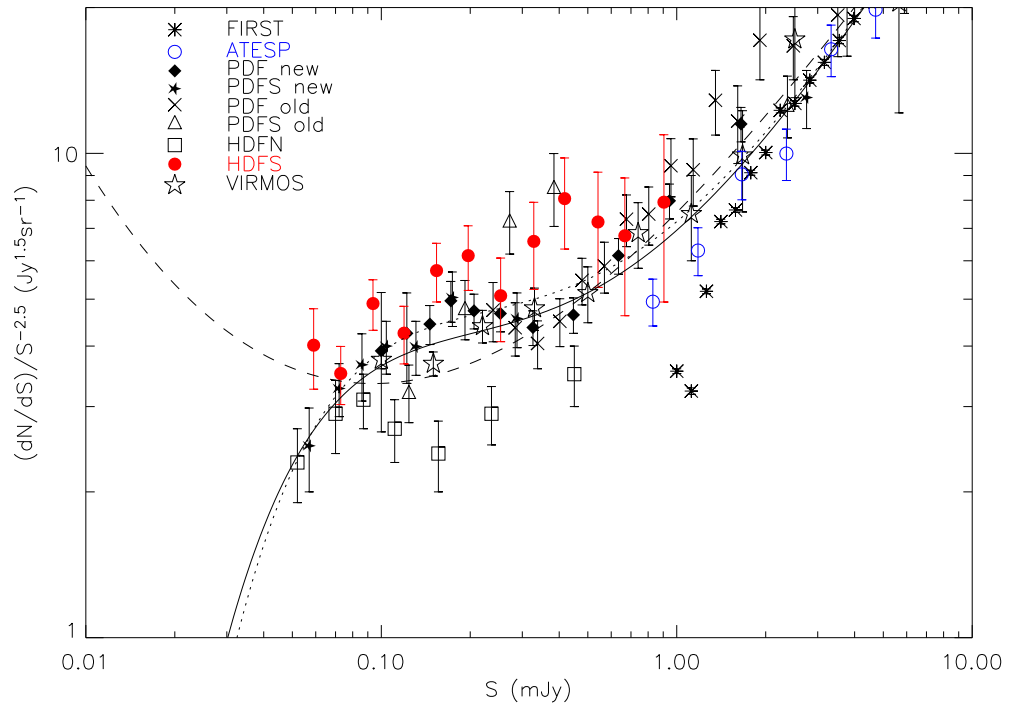


Fig. 20.— Normalised 1.4 GHz differential radio source counts - zoomed on the faint flux density end. Symbols and lines are the same as Figure 19.

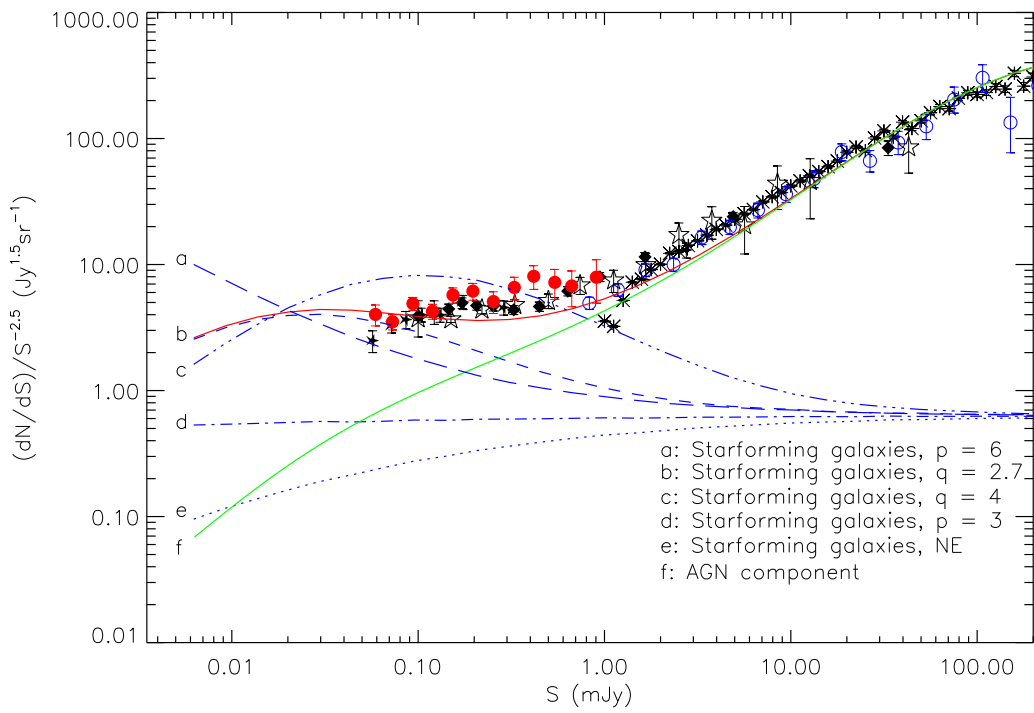


Fig. 21.— Radio source count models, plotted with observed data. The observed counts are as for Figure 19. See Section 7.2 for a description of the models. The solid line near “b” is just model “b” added to the AGN component (line “f”).

Table 1. ATHDFS 1.4 GHz catalogue

ID	source	RA	σ_α	Dec	σ_δ	S_{peak}	S_{int}	θ_{maj}	θ_{min}	PA	SN _{local}	Flag	Notes
1	ATHDFS_J223303.6-605751	22:33:03.62	0.12	-60:57:51.6	0.41	0.297	0.508	0.00	0.00	0.0	16.4	2	
2	ATHDFS_J223325.8-605729	22:33:25.88	0.55	-60:57:29.3	1.28	0.092	0.162	7.81	5.90	-5.3	5.1	2	
3	ATHDFS_J223255.6-605656	22:32:55.62	0.48	-60:56:56.5	0.76	0.159	0.375	9.35	6.32	-0.5	7.7	2	
4	ATHDFS_J223246.3-605654	22:32:46.30	0.28	-60:56:54.0	0.50	0.170	0.254	6.92	2.24	18.6	10.0	2	
5	ATHDFS_J223403.4-605640	22:34:03.43	0.54	-60:56:40.3	0.66	0.126	0.210	5.63	5.20	-7.8	6.6	2	
6	ATHDFS_J223243.8-605608	22:32:43.80	0.60	-60:56:08.8	0.62	0.149	0.363	8.55	7.33	57.1	7.8	1	ATHDFS_J223244.8-605603
7	ATHDFS_J223244.8-605603	22:32:44.89	0.43	-60:56:03.7	0.84	0.119	0.176	7.41	1.01	19.2	6.2	1	ATHDFS_J223243.8-605608
8	ATHDFS_J223410.5-605545	22:34:10.58	0.05	-60:55:45.4	0.09	1.284	2.106	7.28	3.47	-3.9	58.7	1	ATHDFS_J223409.5-605559
9	ATHDFS_J223409.5-605559	22:34:09.50	0.05	-60:55:59.6	0.10	1.302	2.443	8.88	3.75	8.6	59.6	1	ATHDFS_J223410.5-605545
10	ATHDFS_J223308.5-605544	22:33:08.50	0.03	-60:55:44.3	0.04	2.056	3.643	6.70	5.06	-1.1	112.2	1	
11	ATHDFS_J223314.6-605543	22:33:14.63	0.40	-60:55:43.5	0.57	0.172	0.322	7.20	5.29	10.3	8.7	2	
12	ATHDFS_J223316.9-605533	22:33:16.98	0.48	-60:55:33.6	0.49	0.187	0.420	7.92	6.85	62.0	9.5	2	
13	ATHDFS_J223353.9-605452	22:33:53.92	0.01	-60:54:52.1	0.02	4.386	5.918	6.05	1.45	-10.5	259.1	1	
14	ATHDFS_J223334.6-605455	22:33:34.67	0.11	-60:54:55.9	0.23	0.339	0.451	0.00	0.00	0.0	21.1	1	
15	ATHDFS_J223214.8-605430	22:32:14.85	0.01	-60:54:30.2	0.01	13.169	18.601	6.57	1.17	26.9	482.9	1	
16	ATHDFS_J223448.4-605417	22:34:48.45	0.08	-60:54:17.5	0.11	0.959	1.396	6.71	1.87	-33.0	41.1	1	
17	ATHDFS_J223317.5-605416	22:33:17.56	0.01	-60:54:16.2	0.01	5.227	7.754	5.91	3.41	-0.7	305.3	1	ATHDFS_J223316.4-605410
18	ATHDFS_J223316.4-605410	22:33:16.46	0.01	-60:54:10.2	0.02	3.465	5.570	6.43	4.03	-11.0	202.4	1	ATHDFS_J223317.5-605416
19	ATHDFS_J223156.0-605417	22:31:56.00	0.25	-60:54:17.3	0.34	0.271	0.341	11.43	5.16	-50.2	12.4	2	
20	ATHDFS_J223204.8-605414	22:32:04.87	0.80	-60:54:14.6	1.01	0.152	0.526	11.70	9.22	21.1	6.1	2	
21	ATHDFS_J223228.8-605406	22:32:28.80	0.31	-60:54:06.5	0.45	0.132	0.159	3.90	2.00	15.8	8.6	2	
22	ATHDFS_J223430.9-605357	22:34:30.90	0.30	-60:53:57.9	0.42	0.159	0.199	3.92	2.78	10.6	9.3	2	
23	ATHDFS_J223230.3-605352	22:32:30.30	0.26	-60:53:52.1	0.47	0.166	0.289	7.70	3.80	10.8	11.4	2	
24	ATHDFS_J223151.1-605328	22:31:51.13	0.49	-60:53:28.1	0.47	0.213	0.316	0.00	0.00	0.0	8.3	2	
25	ATHDFS_J223145.4-605311	22:31:45.49	0.25	-60:53:11.3	0.31	0.334	0.589	8.00	3.39	40.5	15.3	2	
26	ATHDFS_J223453.4-605259	22:34:53.47	0.23	-60:52:59.9	0.30	0.293	0.483	7.64	2.96	-36.1	15.9	2	
27	ATHDFS_J223141.5-605302	22:31:41.51	0.93	-60:53:02.1	0.86	0.113	0.204	9.67	0.28	51.6	5.3	2	
28	ATHDFS_J223150.6-605258	22:31:50.63	0.35	-60:52:58.1	0.55	0.222	0.315	6.79	0.47	29.2	8.5	2	
29	ATHDFS_J223203.0-605242	22:32:03.02	0.00	-60:52:42.9	0.00	62.635	87.888	6.30	1.41	33.3	1579.3	1	ATHDFS_J223201.8-605225
30	ATHDFS_J223201.8-605225	22:32:01.80	0.79	-60:52:25.8	0.71	0.446	1.239	16.47	1.20	49.8	8.9	1	ATHDFS_J223203.0-605242
31	ATHDFS_J223301.5-605250	22:33:01.52	0.19	-60:52:50.6	0.33	0.223	0.404	7.75	4.36	-0.4	16.4	1	ATHDFS_J223301.1-605239
32	ATHDFS_J223301.1-605239	22:33:01.12	0.29	-60:52:39.9	0.39	0.175	0.335	7.76	5.07	-30.4	12.8	1	ATHDFS_J223301.5-605250
33	ATHDFS_J223458.6-605225	22:34:58.63	0.02	-60:52:25.1	0.03	3.300	5.440	7.71	2.89	-33.6	160.7	1	
34	ATHDFS_J223345.4-605227	22:33:45.46	0.35	-60:52:27.4	0.54	0.107	0.111	0.00	0.00	0.0	6.9	2	
35	ATHDFS_J223454.9-605211	22:34:54.95	0.02	-60:52:11.4	0.03	3.556	5.062	6.29	2.01	-35.9	174.5	1	
36	ATHDFS_J223352.5-605210	22:33:52.50	0.34	-60:52:10.5	0.40	0.138	0.157	0.00	0.00	0.0	8.4	2	
37	ATHDFS_J223241.8-605209	22:32:41.85	0.39	-60:52:09.3	0.70	0.088	0.094	0.00	0.00	0.0	5.6	2	
38	ATHDFS_J223242.9-605155	22:32:42.95	0.36	-60:51:55.7	0.64	0.103	0.114	0.00	0.00	0.0	6.3	2	
39	ATHDFS_J223223.3-605137	22:32:23.33	0.03	-60:51:37.9	0.05	1.523	2.079	5.64	2.06	28.4	92.9	1	
40	ATHDFS_J223323.8-605141	22:33:23.89	0.34	-60:51:41.5	0.31	0.114	0.114	0.00	0.00	0.0	8.9	2	
41	ATHDFS_J223420.1-605138	22:34:20.12	0.59	-60:51:38.9	0.79	0.072	0.094	0.00	0.00	0.0	5.0	2	
42	ATHDFS_J223427.0-605132	22:34:27.08	0.64	-60:51:32.9	0.70	0.095	0.172	8.35	3.45	-45.9	6.6	2	
43	ATHDFS_J223238.8-605113	22:32:38.89	0.31	-60:51:13.8	0.54	0.086	0.063	0.00	0.00	0.0	5.3	2	
44	ATHDFS_J223403.1-605101	22:34:03.19	0.01	-60:51:01.8	0.01	9.569	12.043	4.82	1.78	-17.2	548.7	1	
45	ATHDFS_J223139.6-605039	22:31:39.62	0.42	-60:50:39.3	0.73	0.125	0.212	8.76	1.92	26.4	7.6	2	
46	ATHDFS_J223257.0-605039	22:32:57.01	0.42	-60:50:39.1	0.52	0.093	0.120	4.59	2.19	40.5	7.3	2	
47	ATHDFS_J223226.9-605029	22:32:26.90	0.63	-60:50:29.4	0.81	0.065	0.094	0.00	0.00	0.0	5.0	2	
48	ATHDFS_J223142.8-605024	22:31:42.80	0.48	-60:50:24.9	0.51	0.148	0.283	8.37	4.18	47.4	9.0	2	
49	ATHDFS_J223238.5-605018	22:32:38.56	0.14	-60:50:18.5	0.17	0.309	0.405	4.27	3.10	31.7	22.2	1	
50	ATHDFS_J223306.7-605014	22:33:06.74	0.20	-60:50:14.7	0.55	0.075	0.056	0.00	0.00	0.0	6.6	2	
51	ATHDFS_J223411.6-604931	22:34:11.61	0.31	-60:49:31.2	0.45	0.123	0.160	4.67	2.60	19.0	9.1	2	

Table 1—Continued

ID	source	RA	σ_α	Dec	σ_δ	S_{peak}	S_{int}	θ_{maj}	θ_{min}	PA	SN_{local}	Flag	Notes
52	ATHDFS_J223329.3–604931	22:33:29.36	0.28	−60:49:31.7	0.42	0.126	0.182	6.00	2.84	−24.6	10.7	2	
53	ATHDFS_J223221.3–604929	22:32:21.37	0.27	−60:49:29.1	0.48	0.083	0.077	0.00	0.00	0.0	7.2	2	
54	ATHDFS_J223223.6–604923	22:32:23.67	0.53	−60:49:23.8	0.86	0.086	0.209	10.71	5.49	−22.6	7.2	2	
55	ATHDFS_J223301.3–604926	22:33:01.31	0.44	−60:49:26.6	0.45	0.074	0.072	0.00	0.00	0.0	6.3	2	
56	ATHDFS_J223414.3–604923	22:34:14.39	0.21	−60:49:23.4	0.34	0.134	0.125	0.00	0.00	0.0	9.8	2	
57	ATHDFS_J223524.8–604918	22:35:24.89	0.40	−60:49:18.6	0.49	0.132	0.136	0.00	0.00	0.0	6.5	2	ATHDFS_J223525.9–604907
58	ATHDFS_J223525.9–604907	22:35:25.98	0.73	−60:49:07.8	0.68	0.142	0.320	9.43	5.42	−56.2	6.8	2	ATHDFS_J223524.8–604918
59	ATHDFS_J223430.0–604922	22:34:30.01	0.81	−60:49:22.1	0.99	0.083	0.172	9.86	3.96	−39.7	5.4	2	
60	ATHDFS_J223454.0–604904	22:34:54.04	0.79	−60:49:04.6	0.86	0.119	0.483	12.51	10.76	−35.9	7.0	2	
61	ATHDFS_J223413.1–604909	22:34:13.15	0.26	−60:49:09.8	0.37	0.145	0.185	4.65	2.29	−26.0	10.8	2	
62	ATHDFS_J223502.1–604858	22:35:02.16	1.20	−60:48:58.6	0.99	0.125	0.423	0.00	0.00	0.0	6.8	n	
63	ATHDFS_J223107.4–604855	22:31:07.48	0.01	−60:48:55.0	0.01	7.200	11.272	7.12	2.11	54.9	375.8	1	
64	ATHDFS_J223400.5–604903	22:34:00.52	0.23	−60:49:03.7	0.33	0.206	0.338	6.62	4.03	21.0	14.3	1	ATHDFS_J223359.3–604901
65	ATHDFS_J223359.3–604901	22:33:59.31	0.28	−60:49:01.4	0.63	0.110	0.193	0.00	0.00	0.0	7.6	1	ATHDFS_J223400.5–604903
66	ATHDFS_J223359.4–604901	22:33:59.41	0.27	−60:49:01.4	0.66	0.114	0.154	0.00	0.00	0.0	7.9	2	
67	ATHDFS_J223417.0–604857	22:34:17.03	0.36	−60:48:57.2	0.41	0.109	0.120	0.00	0.00	0.0	8.1	2	
68	ATHDFS_J223543.9–604838	22:35:43.90	0.16	−60:48:38.6	0.16	0.407	0.614	6.54	2.49	−55.0	24.2	1	
69	ATHDFS_J223407.5–604847	22:34:07.53	0.41	−60:48:47.6	0.61	0.079	0.068	0.00	0.00	0.0	5.3	2	
70	ATHDFS_J223235.6–604844	22:32:35.65	0.22	−60:48:44.7	0.45	0.101	0.103	0.00	0.00	0.0	9.0	2	
71	ATHDFS_J223447.4–604843	22:34:47.48	0.28	−60:48:43.6	0.56	0.091	0.089	0.00	0.00	0.0	6.9	2	
72	ATHDFS_J223452.0–604834	22:34:52.03	0.24	−60:48:34.4	0.34	0.179	0.245	5.10	2.93	−21.9	12.3	2	
73	ATHDFS_J223337.8–604833	22:33:37.83	0.11	−60:48:33.9	0.17	0.265	0.322	4.35	1.74	−11.4	24.2	1	
74	ATHDFS_J223146.9–604827	22:31:46.97	0.82	−60:48:27.9	0.69	0.083	0.120	0.00	0.00	0.0	5.2	2	
75	ATHDFS_J223255.7–604823	22:32:55.77	0.26	−60:48:23.4	0.40	0.107	0.125	0.00	0.00	0.0	9.9	2	
76	ATHDFS_J223250.5–604814	22:32:50.50	0.20	−60:48:14.8	0.38	0.103	0.093	0.00	0.00	0.0	9.5	2	
77	ATHDFS_J223109.5–604810	22:31:09.56	0.69	−60:48:10.5	0.71	0.113	0.205	7.37	4.47	52.7	6.0	2	
78	ATHDFS_J223359.7–604806	22:33:59.72	0.38	−60:48:06.3	0.72	0.090	0.103	0.00	0.00	0.0	6.1	2	
79	ATHDFS_J223243.0–604758	22:32:43.04	0.45	−60:47:58.8	0.63	0.072	0.080	0.00	0.00	0.0	5.8	2	
80	ATHDFS_J223414.7–604753	22:34:14.73	0.14	−60:47:53.9	0.16	0.323	0.410	3.58	3.25	89.6	22.7	1	
81	ATHDFS_J223217.6–604751	22:32:17.63	0.79	−60:47:51.6	0.61	0.069	0.082	0.00	0.00	0.0	5.2	2	
82	ATHDFS_J223417.5–604749	22:34:17.50	0.48	−60:47:49.0	0.60	0.070	0.062	0.00	0.00	0.0	5.0	2	
83	ATHDFS_J223226.8–604745	22:32:26.84	0.17	−60:47:45.5	0.27	0.158	0.186	0.00	0.00	0.0	15.3	1	
84	ATHDFS_J223254.0–604736	22:32:54.06	0.08	−60:47:36.8	0.13	0.304	0.336	3.30	0.43	3.3	29.4	1	
85	ATHDFS_J223340.2–604730	22:33:40.22	0.69	−60:47:30.7	0.63	0.060	0.065	0.00	0.00	0.0	5.1	2	
86	ATHDFS_J223141.7–604725	22:31:41.79	0.53	−60:47:25.7	0.54	0.101	0.137	5.08	2.44	61.0	6.5	2	
87	ATHDFS_J223353.3–604723	22:33:53.32	0.54	−60:47:23.6	0.68	0.070	0.075	0.00	0.00	0.0	5.1	2	
88	ATHDFS_J223527.5–604714	22:35:27.50	0.34	−60:47:14.1	0.53	0.203	0.334	6.66	4.16	−8.3	9.2	2	
89	ATHDFS_J223444.0–604710	22:34:44.00	0.30	−60:47:10.8	0.49	0.150	0.251	8.44	2.29	−27.5	11.1	2	
90	ATHDFS_J223108.1–604706	22:31:08.16	0.56	−60:47:06.9	0.79	0.110	0.192	7.01	4.58	−22.5	6.1	2	
91	ATHDFS_J223315.8–604707	22:33:15.84	0.53	−60:47:07.1	0.61	0.064	0.073	0.00	0.00	0.0	6.0	2	
92	ATHDFS_J223420.4–604658	22:34:20.47	0.29	−60:46:58.9	0.35	0.141	0.155	0.00	0.00	0.0	9.4	2	
93	ATHDFS_J223527.8–604639	22:35:27.84	0.02	−60:46:39.3	0.02	3.626	5.478	6.17	3.01	−60.4	191.9	1	ATHDFS_J223527.3–604647
94	ATHDFS_J223527.3–604647	22:35:27.35	0.09	−60:46:47.3	0.09	0.837	1.423	6.63	4.38	−55.6	44.3	1	ATHDFS_J223527.8–604639
95	ATHDFS_J223231.6–604654	22:32:31.69	0.29	−60:46:54.2	0.59	0.066	0.053	0.00	0.00	0.0	5.6	2	
96	ATHDFS_J223254.0–604650	22:32:54.02	0.32	−60:46:50.6	0.41	0.114	0.140	0.00	0.00	0.0	9.5	2	
97	ATHDFS_J223147.2–604647	22:31:47.29	0.44	−60:46:47.9	0.65	0.071	0.077	0.00	0.00	0.0	5.6	2	
98	ATHDFS_J223305.3–604647	22:33:05.31	0.47	−60:46:47.2	0.97	0.056	0.086	0.00	0.00	0.0	5.5	2	
99	ATHDFS_J223118.9–604644	22:31:18.99	0.48	−60:46:44.0	0.36	0.135	0.174	0.00	0.00	0.0	8.3	2	
100	ATHDFS_J223333.2–604642	22:33:33.20	0.12	−60:46:42.8	0.20	0.234	0.255	0.00	0.00	0.0	19.4	1	
101	ATHDFS_J223300.3–604640	22:33:00.32	0.29	−60:46:40.8	0.70	0.084	0.104	0.00	0.00	0.0	7.1	2	
102	ATHDFS_J223228.5–604642	22:32:28.53	0.52	−60:46:42.6	0.77	0.065	0.077	0.00	0.00	0.0	5.0	2	

Table 1—Continued

ID	source	RA	σ_α	Dec	σ_δ	S_{peak}	S_{int}	θ_{maj}	θ_{min}	PA	SN_{local}	Flag	Notes
103	ATHDFS_J223536.8–604632	22:35:36.87	0.28	−60:46:32.7	0.22	0.310	0.568	7.94	3.88	−69.0	17.4	1	
104	ATHDFS_J223312.3–604630	22:33:12.39	0.40	−60:46:30.6	0.45	0.086	0.079	0.00	0.00	0.0	6.5	2	
105	ATHDFS_J223330.4–604624	22:33:30.48	0.24	−60:46:24.4	0.43	0.105	0.113	0.00	0.00	0.0	9.2	2	
106	ATHDFS_J223434.7–604603	22:34:34.72	0.44	−60:46:03.0	0.73	0.099	0.147	6.27	2.94	−16.1	6.5	2	
107	ATHDFS_J223310.2–604601	22:33:10.29	0.50	−60:46:01.3	1.05	0.060	0.090	0.00	0.00	0.0	5.2	2	
108	ATHDFS_J223258.6–604548	22:32:58.62	0.35	−60:45:48.8	0.66	0.082	0.110	6.09	0.71	17.4	7.1	2	
109	ATHDFS_J223329.6–604537	22:33:29.69	0.58	−60:45:37.4	0.82	0.102	0.272	10.75	6.62	−26.1	7.3	2	
110	ATHDFS_J223408.1–604534	22:34:08.13	0.23	−60:45:34.6	0.27	0.171	0.181	0.00	0.00	0.0	12.0	2	
111	ATHDFS_J223342.9–604524	22:33:42.92	0.02	−60:45:24.8	0.03	1.826	1.968	2.63	0.90	−15.4	128.9	1	
112	ATHDFS_J223324.0–604516	22:33:24.08	0.77	−60:45:16.2	0.40	0.134	0.284	0.00	0.00	0.0	8.9	2	
113	ATHDFS_J223320.1–604457	22:33:20.15	0.37	−60:44:57.4	0.65	0.148	0.344	10.05	5.54	12.4	9.4	2	
114	ATHDFS_J223443.3–604452	22:34:43.38	0.03	−60:44:52.7	0.04	1.329	1.534	3.59	1.16	−48.4	84.6	1	
115	ATHDFS_J223121.4–604448	22:31:21.45	0.64	−60:44:48.5	1.04	0.077	0.131	0.00	0.00	0.0	5.0	2	
116	ATHDFS_J223311.5–604449	22:33:11.53	0.26	−60:44:49.7	0.23	0.175	0.261	5.78	3.14	71.8	15.3	2	
117	ATHDFS_J223319.1–604428	22:33:19.12	0.01	−60:44:28.2	0.01	5.589	6.230	3.44	0.33	10.2	301.9	1	
118	ATHDFS_J223210.3–604433	22:32:10.36	0.00	−60:44:33.0	0.00	40.156	56.513	4.41	4.00	75.2	1242.1	1	
119	ATHDFS_J223439.0–604435	22:34:39.08	0.25	−60:44:35.4	0.32	0.166	0.184	0.00	0.00	0.0	10.8	2	
120	ATHDFS_J223356.9–604438	22:33:56.94	0.58	−60:44:38.9	0.42	0.085	0.076	0.00	0.00	0.0	5.2	2	
121	ATHDFS_J223244.1–604437	22:32:44.10	0.38	−60:44:37.3	0.23	0.102	0.118	0.00	0.00	0.0	10.5	2	
122	ATHDFS_J223147.2–604415	22:31:47.29	0.64	−60:44:15.2	0.64	0.076	0.091	0.00	0.00	0.0	5.0	2	
123	ATHDFS_J223326.3–604416	22:33:26.38	0.44	−60:44:16.4	0.58	0.077	0.089	0.00	0.00	0.0	6.2	2	
124	ATHDFS_J223255.2–604415	22:32:55.26	0.47	−60:44:15.7	0.59	0.069	0.069	0.00	0.00	0.0	5.4	2	
125	ATHDFS_J223422.4–604412	22:34:22.41	0.52	−60:44:12.0	0.49	0.098	0.130	4.96	2.03	70.0	6.9	2	
126	ATHDFS_J223226.8–604408	22:32:26.88	0.31	−60:44:08.8	0.68	0.100	0.133	0.00	0.00	0.0	7.3	2	
127	ATHDFS_J223313.9–604359	22:33:13.90	0.53	−60:43:59.8	0.53	0.103	0.175	6.32	4.66	−65.0	7.5	2	
128	ATHDFS_J223255.6–604400	22:32:55.65	0.24	−60:44:00.1	0.32	0.101	0.072	0.00	0.00	0.0	7.7	2	
129	ATHDFS_J223101.3–604351	22:31:01.30	0.43	−60:43:51.4	0.28	0.138	0.159	0.00	0.00	0.0	9.0	2	
130	ATHDFS_J223319.1–604348	22:33:19.13	0.04	−60:43:48.6	0.06	1.022	1.085	2.29	0.84	5.8	63.5	1	
131	ATHDFS_J223147.4–604338	22:31:47.48	0.32	−60:43:38.2	0.37	0.135	0.176	4.00	3.30	63.2	9.9	2	
132	ATHDFS_J223126.2–604337	22:31:26.24	0.37	−60:43:37.3	0.32	0.128	0.174	5.15	2.19	82.9	10.1	2	
133	ATHDFS_J223439.7–604337	22:34:39.73	0.61	−60:43:37.3	0.93	0.096	0.211	10.18	4.58	−28.5	6.3	2	
134	ATHDFS_J223534.3–604328	22:35:34.32	0.15	−60:43:28.9	0.12	0.435	0.657	6.48	2.32	−76.4	28.1	1	
135	ATHDFS_J223250.6–604336	22:32:50.62	0.35	−60:43:36.5	0.53	0.086	0.105	0.00	0.00	0.0	7.5	2	
136	ATHDFS_J223522.2–604326	22:35:22.26	0.53	−60:43:26.9	0.71	0.114	0.222	7.35	5.64	−15.1	6.9	2	
137	ATHDFS_J223330.4–604332	22:33:30.46	0.35	−60:43:32.5	0.37	0.080	0.063	0.00	0.00	0.0	6.6	2	
138	ATHDFS_J223355.6–604315	22:33:55.63	0.00	−60:43:15.7	0.00	144.700	154.700	2.27	1.18	−19.2	3291.6	1	
139	ATHDFS_J223440.4–604309	22:34:40.46	0.53	−60:43:09.9	0.48	0.106	0.150	5.28	2.94	78.4	7.1	2	
140	ATHDFS_J223430.8–604310	22:34:30.82	0.48	−60:43:10.4	0.95	0.094	0.141	0.00	0.00	0.0	5.4	2	
141	ATHDFS_J223240.2–604306	22:32:40.24	0.21	−60:43:06.5	0.45	0.091	0.082	0.00	0.00	0.0	8.4	2	
142	ATHDFS_J223207.9–604305	22:32:07.96	0.45	−60:43:05.6	0.33	0.102	0.114	0.00	0.00	0.0	8.2	2	
143	ATHDFS_J223427.3–604258	22:34:27.33	0.10	−60:42:58.9	0.13	0.507	0.571	3.37	0.82	−40.4	28.0	1	
144	ATHDFS_J223130.4–604232	22:31:30.45	0.49	−60:42:32.3	0.70	0.110	0.235	8.26	5.99	7.7	7.6	2	
145	ATHDFS_J223425.8–604232	22:34:25.82	0.59	−60:42:32.7	0.61	0.099	0.137	0.00	0.00	0.0	5.9	2	
146	ATHDFS_J223239.0–604230	22:32:39.04	0.80	−60:42:30.1	0.33	0.056	0.055	0.00	0.00	0.0	5.2	2	
147	ATHDFS_J223312.4–604227	22:33:12.45	0.46	−60:42:27.2	0.45	0.078	0.068	0.00	0.00	0.0	5.6	2	
148	ATHDFS_J223437.2–604214	22:34:37.27	0.02	−60:42:14.3	0.02	2.300	2.872	3.86	2.52	79.5	161.2	1	
149	ATHDFS_J223508.5–604217	22:35:08.52	0.47	−60:42:17.5	0.48	0.124	0.173	4.86	3.31	68.6	7.5	2	
150	ATHDFS_J223338.8–604216	22:33:38.89	0.28	−60:42:16.4	0.37	0.150	0.168	0.00	0.00	0.0	9.6	2	
151	ATHDFS_J223523.6–604207	22:35:23.69	0.09	−60:42:07.9	0.08	0.583	0.723	0.00	0.00	0.0	39.9	1	
152	ATHDFS_J223135.8–604207	22:31:35.84	0.67	−60:42:07.0	0.34	0.087	0.113	0.00	0.00	0.0	7.2	2	
153	ATHDFS_J223359.8–604155	22:33:59.86	0.30	−60:41:55.6	0.39	0.260	0.536	7.50	6.22	2.5	13.0	2	

Table 1—Continued

ID	source	RA	σ_α	Dec	σ_δ	S_{peak}	S_{int}	θ_{maj}	θ_{min}	PA	SN_{local}	Flag	Notes
154	ATHDFS_J223255.4–604151	22:32:55.45	0.23	−60:41:51.3	0.35	0.125	0.132	0.00	0.00	0.0	10.4	2	
155	ATHDFS_J223158.4–604142	22:31:58.45	0.37	−60:41:42.3	0.35	0.106	0.111	0.00	0.00	0.0	8.4	2	
156	ATHDFS_J223339.5–604131	22:33:39.59	0.28	−60:41:31.1	0.49	0.094	0.083	0.00	0.00	0.0	6.9	2	
157	ATHDFS_J223224.5–604113	22:32:24.52	0.01	−60:41:13.0	0.01	3.711	4.108	2.89	0.83	60.6	292.2	1	
158	ATHDFS_J223206.5–604102	22:32:06.53	0.64	−60:41:02.2	0.57	0.063	0.073	0.00	0.00	0.0	5.2	2	
159	ATHDFS_J223448.3–604042	22:34:48.33	0.10	−60:40:42.8	0.10	0.345	0.437	4.32	2.06	−87.6	32.8	1	
160	ATHDFS_J223430.1–604043	22:34:30.13	0.44	−60:40:43.5	0.46	0.057	0.045	0.00	0.00	0.0	5.3	2	
161	ATHDFS_J223251.1–604042	22:32:51.14	0.34	−60:40:42.1	0.45	0.070	0.065	0.00	0.00	0.0	6.9	2	
162	ATHDFS_J223514.4–604024	22:35:14.48	0.21	−60:40:24.8	0.18	0.199	0.238	0.00	0.00	0.0	16.6	1	
163	ATHDFS_J223348.2–604026	22:33:48.25	0.45	−60:40:26.7	0.38	0.097	0.094	0.00	0.00	0.0	6.8	2	
164	ATHDFS_J223429.8–604020	22:34:29.84	0.37	−60:40:20.2	0.34	0.092	0.099	0.00	0.00	0.0	9.1	2	
165	ATHDFS_J223417.8–604009	22:34:17.80	0.02	−60:40:09.3	0.03	1.419	1.502	0.00	0.00	0.0	110.0	1	
166	ATHDFS_J223337.5–604006	22:33:37.53	0.22	−60:40:06.6	0.44	0.094	0.081	0.00	0.00	0.0	8.0	2	
167	ATHDFS_J223412.2–603957	22:34:12.22	0.40	−60:39:57.3	0.36	0.083	0.082	0.00	0.00	0.0	7.3	2	
168	ATHDFS_J223438.0–603951	22:34:38.07	0.34	−60:39:51.2	0.46	0.091	0.102	0.00	0.00	0.0	7.9	2	
169	ATHDFS_J223343.9–603953	22:33:43.91	0.38	−60:39:53.6	1.03	0.073	0.102	0.00	0.00	0.0	5.4	2	
170	ATHDFS_J223047.9–603933	22:30:47.91	0.47	−60:39:33.7	0.34	0.163	0.239	6.19	2.05	87.3	9.2	2	
171	ATHDFS_J223324.7–603934	22:33:24.71	0.32	−60:39:34.6	0.38	0.089	0.092	0.00	0.00	0.0	8.5	2	
172	ATHDFS_J223220.6–603931	22:32:20.60	0.18	−60:39:31.8	0.23	0.138	0.136	0.00	0.00	0.0	13.5	1	
173	ATHDFS_J223529.2–603927	22:35:29.20	0.26	−60:39:27.0	0.22	0.179	0.229	4.97	0.93	−73.5	14.2	1	
174	ATHDFS_J223400.2–603930	22:34:00.27	0.39	−60:39:30.4	0.41	0.104	0.117	0.00	0.00	0.0	8.2	2	
175	ATHDFS_J223207.9–603928	22:32:07.99	0.33	−60:39:28.7	0.37	0.098	0.107	0.00	0.00	0.0	8.7	2	
176	ATHDFS_J223222.7–603924	22:32:22.72	0.92	−60:39:24.4	0.73	0.054	0.086	0.00	0.00	0.0	5.4	2	
177	ATHDFS_J223253.7–603921	22:32:53.70	0.69	−60:39:21.2	0.62	0.052	0.050	0.00	0.00	0.0	5.1	2	
178	ATHDFS_J223331.3–603914	22:33:31.32	0.67	−60:39:14.6	0.82	0.076	0.099	0.00	0.00	0.0	5.7	2	
179	ATHDFS_J223123.1–603903	22:31:23.18	0.01	−60:39:03.5	0.00	17.618	23.988	5.24	2.05	84.8	719.4	1	
180	ATHDFS_J223258.7–603903	22:32:58.79	0.36	−60:39:03.9	0.47	0.058	0.043	0.00	0.00	0.0	5.7	2	
181	ATHDFS_J223245.6–603857	22:32:45.65	0.03	−60:38:57.3	0.04	0.794	0.843	2.27	0.73	30.5	75.9	1	
182	ATHDFS_J223205.9–603857	22:32:05.99	0.15	−60:38:57.0	0.13	0.254	0.286	0.00	0.00	0.0	22.2	1	
183	ATHDFS_J223144.4–603858	22:31:44.45	0.80	−60:38:58.4	0.66	0.068	0.107	0.00	0.00	0.0	5.3	2	
184	ATHDFS_J223153.7–603853	22:31:53.74	0.31	−60:38:53.6	0.33	0.076	0.059	0.00	0.00	0.0	7.3	2	
185	ATHDFS_J223450.4–603844	22:34:50.40	0.27	−60:38:44.9	0.28	0.154	0.212	5.48	2.24	−56.9	13.1	1	
186	ATHDFS_J223307.1–603846	22:33:07.13	0.30	−60:38:46.9	0.46	0.106	0.137	4.90	2.15	17.0	9.0	2	
187	ATHDFS_J223457.3–603840	22:34:57.30	0.48	−60:38:40.2	0.65	0.096	0.184	7.09	5.66	4.0	7.5	2	
188	ATHDFS_J223232.3–603842	22:32:32.32	0.43	−60:38:42.3	0.36	0.083	0.085	0.00	0.00	0.0	7.3	2	
189	ATHDFS_J223505.5–603825	22:35:05.53	0.14	−60:38:25.9	0.13	0.282	0.343	4.06	1.32	83.9	23.6	1	
190	ATHDFS_J223304.6–603835	22:33:04.66	0.52	−60:38:35.8	0.52	0.067	0.067	0.00	0.00	0.0	5.6	2	
191	ATHDFS_J223608.1–603823	22:36:08.12	1.22	−60:38:23.9	0.69	0.103	0.258	11.96	4.21	72.7	5.4	2	
192	ATHDFS_J223432.1–603815	22:34:32.10	0.24	−60:38:15.4	0.37	0.159	0.268	6.82	4.24	12.5	13.1	1	
193	ATHDFS_J223138.7–603818	22:31:38.74	0.35	−60:38:18.5	0.47	0.087	0.089	0.00	0.00	0.0	7.2	2	
194	ATHDFS_J223418.6–603808	22:34:18.63	0.07	−60:38:08.0	0.10	0.339	0.346	0.00	0.00	0.0	32.7	1	
195	ATHDFS_J223442.7–603802	22:34:42.70	0.27	−60:38:02.4	0.29	0.163	0.254	5.62	4.26	−57.7	13.5	1	
196	ATHDFS_J223248.2–603805	22:32:48.29	0.33	−60:38:05.6	0.44	0.076	0.076	0.00	0.00	0.0	7.4	2	
197	ATHDFS_J223334.4–603804	22:33:34.47	0.76	−60:38:04.7	0.71	0.055	0.064	0.00	0.00	0.0	5.3	2	
198	ATHDFS_J223436.9–603754	22:34:36.90	0.07	−60:37:54.6	0.08	0.509	0.553	0.00	0.00	0.0	38.3	1	
199	ATHDFS_J223254.5–603748	22:32:54.53	0.38	−60:37:48.0	0.48	0.074	0.092	3.85	2.43	42.4	7.7	2	
200	ATHDFS_J223350.0–603741	22:33:50.09	0.11	−60:37:41.3	0.10	0.448	0.670	6.56	2.22	−58.3	35.5	1	
201	ATHDFS_J223441.6–603740	22:34:41.61	0.25	−60:37:40.3	0.19	0.167	0.194	0.00	0.00	0.0	14.5	1	
202	ATHDFS_J223232.8–603737	22:32:32.85	0.06	−60:37:37.1	0.08	0.544	0.645	3.63	2.00	19.6	45.8	1	
203	ATHDFS_J223142.5–603737	22:31:42.51	0.22	−60:37:37.4	0.23	0.170	0.213	4.04	2.25	77.1	14.6	1	
204	ATHDFS_J223404.8–603732	22:34:04.84	0.02	−60:37:32.3	0.02	2.412	3.238	4.93	2.33	−88.3	193.0	1	

Table 1—Continued

ID	source	RA	σ_α	Dec	σ_δ	S_{peak}	S_{int}	θ_{maj}	θ_{min}	PA	SN_{local}	Flag	Notes
205	ATHDFS_J223503.2-603729	22:35:03.21	0.33	-60:37:29.2	0.41	0.064	0.044	0.00	0.00	0.0	5.7	2	
206	ATHDFS_J223437.7-603726	22:34:37.73	0.23	-60:37:26.5	0.24	0.162	0.187	3.55	1.04	-70.7	13.4	2	
207	ATHDFS_J223417.1-603724	22:34:17.18	0.25	-60:37:24.5	0.33	0.121	0.157	4.13	3.12	-17.7	11.7	2	
208	ATHDFS_J223341.2-603724	22:33:41.20	0.51	-60:37:24.7	0.62	0.065	0.071	0.00	0.00	0.0	5.4	2	
209	ATHDFS_J223225.6-603717	22:32:25.68	0.36	-60:37:17.4	0.84	0.057	0.061	0.00	0.00	0.0	5.3	2	
210	ATHDFS_J223202.5-603714	22:32:02.55	0.20	-60:37:14.0	0.22	0.148	0.151	0.00	0.00	0.0	13.8	1	
211	ATHDFS_J223326.0-603716	22:33:26.01	0.49	-60:37:16.7	0.95	0.061	0.083	0.00	0.00	0.0	5.0	2	
212	ATHDFS_J223506.5-603700	22:35:06.52	1.01	-60:37:00.3	0.81	0.054	0.088	0.00	0.00	0.0	5.1	2	
213	ATHDFS_J223400.2-603653	22:34:00.29	0.02	-60:36:53.3	0.03	1.810	2.209	3.95	2.25	16.5	147.1	1	
214	ATHDFS_J223525.8-603652	22:35:25.88	0.34	-60:36:52.0	0.48	0.106	0.135	4.24	2.83	-14.4	8.3	2	
215	ATHDFS_J223343.7-603651	22:33:43.76	0.39	-60:36:51.5	0.60	0.070	0.070	0.00	0.00	0.0	5.8	2	
216	ATHDFS_J223404.3-603638	22:34:04.36	0.04	-60:36:38.8	0.05	0.914	1.050	2.89	2.24	-26.3	67.5	1	
217	ATHDFS_J223158.1-603636	22:31:58.14	0.27	-60:36:36.7	0.31	0.126	0.173	4.57	3.42	-55.0	12.1	1	
218	ATHDFS_J223605.7-603631	22:36:05.78	1.13	-60:36:31.0	0.57	0.088	0.148	0.00	0.00	0.0	5.3	2	
219	ATHDFS_J223406.7-603637	22:34:06.76	0.43	-60:36:37.6	0.43	0.099	0.127	4.29	2.50	-86.0	7.8	2	
220	ATHDFS_J223054.4-603631	22:30:54.42	0.64	-60:36:31.5	0.60	0.109	0.177	5.99	4.27	83.4	6.3	2	
221	ATHDFS_J223439.9-603629	22:34:39.95	0.14	-60:36:29.7	0.23	0.252	0.407	7.12	3.40	-16.4	21.9	1	
222	ATHDFS_J223341.9-603634	22:33:41.93	0.24	-60:36:34.5	0.36	0.138	0.174	0.00	0.00	0.0	11.7	1	
223	ATHDFS_J223451.7-603632	22:34:51.76	0.29	-60:36:32.9	0.27	0.066	0.039	0.00	0.00	0.0	6.6	2	
224	ATHDFS_J223429.9-603629	22:34:29.97	0.04	-60:36:29.6	0.05	0.608	0.671	2.88	0.47	78.3	69.3	1	
225	ATHDFS_J223316.5-603627	22:33:16.55	0.05	-60:36:27.5	0.05	0.649	0.661	0.00	0.00	0.0	56.2	1	
226	ATHDFS_J223526.2-603617	22:35:26.21	0.44	-60:36:17.6	0.43	0.123	0.190	5.88	3.71	-66.1	8.8	2	
227	ATHDFS_J223518.7-603619	22:35:18.73	0.77	-60:36:19.9	0.42	0.077	0.094	0.00	0.00	0.0	5.8	2	
228	ATHDFS_J223456.2-603619	22:34:56.21	0.34	-60:36:19.2	0.27	0.104	0.120	0.00	0.00	0.0	10.2	2	
229	ATHDFS_J223158.5-603614	22:31:58.59	0.63	-60:36:14.1	0.60	0.061	0.094	6.66	2.54	56.6	6.3	2	
230	ATHDFS_J223410.3-603613	22:34:10.31	0.31	-60:36:13.4	0.39	0.088	0.088	0.00	0.00	0.0	8.1	2	
231	ATHDFS_J223421.8-603603	22:34:21.85	0.55	-60:36:03.8	0.47	0.062	0.068	0.00	0.00	0.0	6.3	2	
232	ATHDFS_J223232.4-603542	22:32:32.40	0.12	-60:35:42.5	0.16	0.299	0.529	6.67	5.03	-9.7	30.0	1	ATHDFS_J223232.5-603553
233	ATHDFS_J223232.5-603553	22:32:32.56	0.12	-60:35:53.1	0.18	0.272	0.466	6.82	4.54	-8.9	27.2	1	ATHDFS_J223232.4-603542
234	ATHDFS_J223104.8-603549	22:31:04.80	0.54	-60:35:49.2	0.48	0.106	0.162	6.55	2.61	-63.1	7.6	2	
235	ATHDFS_J223525.7-603544	22:35:25.76	0.26	-60:35:44.2	0.24	0.230	0.415	6.99	4.72	67.3	16.9	1	
236	ATHDFS_J223229.8-603544	22:32:29.89	0.35	-60:35:44.9	0.45	0.077	0.087	0.00	0.00	0.0	7.9	2	
237	ATHDFS_J223224.0-603537	22:32:24.02	0.03	-60:35:37.7	0.04	1.056	1.259	3.53	2.27	-32.3	97.1	1	
238	ATHDFS_J223253.0-603539	22:32:53.09	0.31	-60:35:39.7	0.31	0.090	0.091	0.00	0.00	0.0	9.2	2	
239	ATHDFS_J223459.4-603535	22:34:59.48	0.36	-60:35:35.7	0.44	0.086	0.094	0.00	0.00	0.0	7.9	2	
240	ATHDFS_J223245.3-603537	22:32:45.34	0.28	-60:35:37.8	0.53	0.051	0.032	0.00	0.00	0.0	5.3	2	
241	ATHDFS_J223046.1-603525	22:30:46.14	0.27	-60:35:25.0	0.25	0.300	0.502	6.42	4.27	73.9	15.2	1	
242	ATHDFS_J223435.5-603532	22:34:35.51	0.33	-60:35:32.1	0.30	0.125	0.149	0.00	0.00	0.0	10.3	2	
243	ATHDFS_J223338.8-603523	22:33:38.84	0.13	-60:35:23.8	0.19	0.185	0.197	0.00	0.00	0.0	18.5	1	
244	ATHDFS_J223208.3-603519	22:32:08.36	0.04	-60:35:19.2	0.04	0.788	0.918	3.23	1.84	-86.4	76.5	1	
245	ATHDFS_J223223.7-603520	22:32:23.70	0.50	-60:35:20.5	0.91	0.068	0.142	9.10	4.98	-4.4	6.4	2	
246	ATHDFS_J223344.9-603515	22:33:44.99	0.13	-60:35:15.6	0.15	0.262	0.344	4.70	2.50	46.9	24.6	1	
247	ATHDFS_J223524.8-603509	22:35:24.81	0.71	-60:35:09.6	0.93	0.066	0.131	8.27	4.93	-32.8	5.4	2	
248	ATHDFS_J223536.3-603506	22:35:36.36	0.67	-60:35:06.4	0.62	0.077	0.101	0.00	0.00	0.0	5.3	2	
249	ATHDFS_J223410.1-603510	22:34:10.19	0.57	-60:35:10.3	0.39	0.064	0.063	0.00	0.00	0.0	6.1	2	
250	ATHDFS_J223549.5-603502	22:35:49.56	0.37	-60:35:02.4	0.37	0.134	0.151	0.00	0.00	0.0	8.4	2	
251	ATHDFS_J223350.5-603503	22:33:50.53	0.03	-60:35:03.9	0.03	1.185	1.252	2.04	0.97	31.7	103.1	1	
252	ATHDFS_J223229.2-603459	22:32:29.21	0.14	-60:34:59.5	0.15	0.192	0.204	0.00	0.00	0.0	20.3	1	ATHDFS_J223230.1-603503
253	ATHDFS_J223230.1-603503	22:32:30.16	0.34	-60:35:03.9	0.24	0.113	0.149	0.00	0.00	0.0	11.9	1	ATHDFS_J223229.2-603459
254	ATHDFS_J223541.5-603454	22:35:41.59	0.37	-60:34:54.7	0.29	0.175	0.274	6.38	3.16	81.5	11.5	1	
255	ATHDFS_J223438.6-603450	22:34:38.60	0.01	-60:34:50.4	0.01	2.875	3.670	4.49	2.11	53.1	286.4	1	

Table 1—Continued

ID	source	RA	σ_α	Dec	σ_δ	S_{peak}	S_{int}	θ_{maj}	θ_{min}	PA	SN_{local}	Flag	Notes
256	ATHDFS_J223103.2-603453	22:31:03.28	0.40	-60:34:53.7	0.44	0.107	0.102	0.00	0.00	0.0	6.7	2	
257	ATHDFS_J223116.4-603452	22:31:16.41	1.15	-60:34:52.0	0.90	0.070	0.149	11.75	1.46	56.0	5.2	2	
258	ATHDFS_J223431.8-603454	22:34:31.81	0.64	-60:34:54.7	0.59	0.066	0.101	6.59	2.52	59.4	6.3	2	
259	ATHDFS_J223425.0-603452	22:34:25.00	0.20	-60:34:52.7	0.24	0.133	0.145	2.06	1.75	67.0	13.7	2	
260	ATHDFS_J223212.3-603448	22:32:12.39	0.54	-60:34:48.7	0.49	0.068	0.093	5.21	2.35	-72.7	6.9	2	
261	ATHDFS_J223307.1-603448	22:33:07.18	0.55	-60:34:48.8	1.08	0.061	0.103	8.75	1.85	20.7	5.3	2	
262	ATHDFS_J223207.4-603445	22:32:07.49	0.40	-60:34:45.8	0.50	0.066	0.062	0.00	0.00	0.0	6.8	2	
263	ATHDFS_J223243.3-603443	22:32:43.34	0.29	-60:34:43.2	0.48	0.063	0.041	0.00	0.00	0.0	5.3	2	
264	ATHDFS_J223410.6-603437	22:34:10.65	0.41	-60:34:37.7	0.43	0.072	0.080	0.00	0.00	0.0	7.3	2	
265	ATHDFS_J223442.8-603433	22:34:42.84	0.41	-60:34:33.9	0.65	0.059	0.068	0.00	0.00	0.0	6.3	2	
266	ATHDFS_J223216.6-603434	22:32:16.63	0.55	-60:34:34.9	0.84	0.052	0.070	0.00	0.00	0.0	5.5	2	
267	ATHDFS_J223539.3-603424	22:35:39.39	0.52	-60:34:24.7	0.46	0.119	0.189	6.33	3.50	69.8	8.0	2	
268	ATHDFS_J223153.2-603422	22:31:53.25	0.27	-60:34:22.8	0.23	0.154	0.221	6.10	1.83	-67.8	15.0	1	
269	ATHDFS_J223401.0-603424	22:34:01.00	0.34	-60:34:24.4	0.44	0.094	0.122	4.03	3.25	28.7	8.7	2	
270	ATHDFS_J223245.5-603419	22:32:45.53	0.12	-60:34:19.1	0.19	0.222	0.265	4.00	1.68	6.7	20.4	1	
271	ATHDFS_J223231.6-603423	22:32:31.69	0.26	-60:34:23.1	0.39	0.070	0.053	0.00	0.00	0.0	7.2	2	
272	ATHDFS_J223055.9-603412	22:30:55.98	0.81	-60:34:12.7	0.63	0.146	0.362	13.73	2.11	55.0	8.1	2	
273	ATHDFS_J223327.6-603414	22:33:27.66	0.06	-60:34:14.1	0.09	0.456	0.455	0.00	0.00	0.0	38.4	1	
274	ATHDFS_J223311.9-603417	22:33:11.97	0.41	-60:34:17.1	0.52	0.059	0.042	0.00	0.00	0.0	5.1	2	
275	ATHDFS_J223434.1-603410	22:34:34.17	0.24	-60:34:10.1	0.35	0.086	0.081	0.00	0.00	0.0	9.3	2	
276	ATHDFS_J223053.2-603402	22:30:53.25	0.56	-60:34:02.9	0.38	0.145	0.233	7.03	2.56	84.6	8.3	2	
277	ATHDFS_J223415.0-603408	22:34:15.00	0.28	-60:34:08.6	0.64	0.054	0.049	0.00	0.00	0.0	5.9	2	
278	ATHDFS_J223529.7-603359	22:35:29.75	0.74	-60:33:59.0	0.89	0.069	0.129	8.73	3.69	-40.6	5.6	2	
279	ATHDFS_J223406.6-603401	22:34:06.69	0.41	-60:34:01.2	0.32	0.112	0.189	6.84	3.76	-86.1	10.9	2	
280	ATHDFS_J223409.7-603402	22:34:09.76	0.28	-60:34:02.5	0.60	0.053	0.037	0.00	0.00	0.0	5.6	2	
281	ATHDFS_J223512.7-603353	22:35:12.76	0.20	-60:33:53.3	0.20	0.129	0.105	0.00	0.00	0.0	12.1	2	
282	ATHDFS_J223306.0-603350	22:33:06.07	0.09	-60:33:50.3	0.13	0.349	0.452	4.45	2.76	11.5	31.2	1	
283	ATHDFS_J223329.7-603352	22:33:29.75	0.25	-60:33:52.1	0.36	0.129	0.152	3.79	1.63	21.7	10.4	2	
284	ATHDFS_J223258.5-603346	22:32:58.59	0.02	-60:33:46.7	0.03	0.942	1.010	2.23	1.33	-16.3	103.9	1	
285	ATHDFS_J223243.4-603352	22:32:43.49	0.22	-60:33:52.0	0.34	0.098	0.085	0.00	0.00	0.0	9.7	2	
286	ATHDFS_J223545.7-603342	22:35:45.76	0.77	-60:33:42.3	0.57	0.079	0.100	0.00	0.00	0.0	5.6	2	
287	ATHDFS_J223138.5-603344	22:31:38.52	0.48	-60:33:44.7	0.51	0.083	0.097	0.00	0.00	0.0	6.4	2	
288	ATHDFS_J223420.9-603336	22:34:20.95	0.01	-60:33:36.5	0.01	3.832	4.328	3.07	1.40	47.6	379.0	1	
289	ATHDFS_J223225.0-603338	22:32:25.05	0.28	-60:33:38.7	0.64	0.080	0.098	0.00	0.00	0.0	7.5	2	
290	ATHDFS_J223513.7-603333	22:35:13.73	0.38	-60:33:33.3	0.41	0.093	0.113	3.93	1.74	59.1	8.2	2	
291	ATHDFS_J223247.6-603337	22:32:47.65	0.42	-60:33:37.0	0.56	0.075	0.082	0.00	0.00	0.0	6.8	2	
292	ATHDFS_J223337.5-603329	22:33:37.57	0.03	-60:33:29.1	0.04	1.038	1.126	2.58	1.22	9.3	88.1	1	
293	ATHDFS_J223253.1-603329	22:32:53.15	0.58	-60:33:29.1	0.71	0.066	0.113	6.36	4.96	-34.4	6.3	2	
294	ATHDFS_J223302.8-603323	22:33:02.83	0.61	-60:33:23.8	0.40	0.051	0.045	0.00	0.00	0.0	5.2	2	
295	ATHDFS_J223509.5-603257	22:35:09.56	0.30	-60:32:57.1	0.21	0.335	0.980	16.11	2.75	57.9	25.4	1	
296	ATHDFS_J223327.9-603304	22:33:27.95	0.13	-60:33:04.8	0.17	0.221	0.234	0.00	0.00	0.0	19.8	1	ATHDFS_J223329.2-603302
297	ATHDFS_J223329.2-603302	22:33:29.28	0.44	-60:33:02.0	0.59	0.059	0.058	0.00	0.00	0.0	5.4	1	ATHDFS_J223327.9-603304
298	ATHDFS_J223339.4-603306	22:33:39.41	0.62	-60:33:06.0	0.32	0.058	0.051	0.00	0.00	0.0	5.6	2	
299	ATHDFS_J223121.6-603301	22:31:21.62	0.71	-60:33:01.1	0.41	0.074	0.075	0.00	0.00	0.0	5.2	2	
300	ATHDFS_J223234.2-603257	22:32:34.27	0.61	-60:32:57.4	0.79	0.057	0.079	0.00	0.00	0.0	6.1	2	
301	ATHDFS_J223308.6-603251	22:33:08.60	0.06	-60:32:51.7	0.08	0.570	0.821	6.59	1.82	-32.6	55.0	1	
302	ATHDFS_J223456.8-603251	22:34:56.81	0.50	-60:32:51.2	0.86	0.061	0.080	0.00	0.00	0.0	5.2	2	
303	ATHDFS_J223323.2-603249	22:33:23.23	0.05	-60:32:49.2	0.07	0.457	0.460	0.00	0.00	0.0	45.9	1	
304	ATHDFS_J223209.7-603253	22:32:09.71	0.58	-60:32:53.9	0.56	0.061	0.051	0.00	0.00	0.0	5.1	2	
305	ATHDFS_J223212.9-603234	22:32:12.90	0.03	-60:32:34.6	0.03	1.770	2.816	7.07	2.77	-54.7	147.3	1	ATHDFS_J223212.9-603243
306	ATHDFS_J223212.9-603243	22:32:12.95	0.04	-60:32:43.3	0.06	0.935	1.466	5.84	4.24	-5.5	77.9	1	ATHDFS_J223212.9-603234

Table 1—Continued

ID	source	RA	σ_α	Dec	σ_δ	S_{peak}	S_{int}	θ_{maj}	θ_{min}	PA	SN_{local}	Flag	Notes
307	ATHDFS_J223229.5–603243	22:32:29.53	0.09	−60:32:43.3	0.15	0.237	0.254	0.00	0.00	0.0	25.1	1	
308	ATHDFS_J223509.4–603235	22:35:09.44	0.10	−60:32:35.9	0.09	0.464	0.583	4.65	0.89	70.2	35.5	1	
309	ATHDFS_J223142.5–603238	22:31:42.59	0.58	−60:32:38.5	0.72	0.071	0.111	5.48	4.46	−30.8	5.9	2	
310	ATHDFS_J223521.1–603235	22:35:21.14	0.56	−60:32:35.5	0.88	0.091	0.192	9.00	5.25	−18.4	6.4	2	
311	ATHDFS_J223317.7–603235	22:33:17.75	0.41	−60:32:35.2	0.38	0.070	0.070	0.00	0.00	0.0	7.3	2	
312	ATHDFS_J223335.3–603234	22:33:35.31	0.35	−60:32:34.5	0.55	0.054	0.045	0.00	0.00	0.0	5.5	2	
313	ATHDFS_J223429.9–603226	22:34:29.99	0.41	−60:32:26.9	0.60	0.059	0.075	0.00	0.00	0.0	6.7	2	
314	ATHDFS_J223331.6–603222	22:33:31.64	0.08	−60:32:22.2	0.11	0.333	0.395	3.31	2.46	2.4	32.4	1	
315	ATHDFS_J223504.4–603221	22:35:04.47	0.40	−60:32:21.1	0.38	0.106	0.129	0.00	0.00	0.0	9.0	2	
316	ATHDFS_J223343.5–603211	22:33:43.56	0.35	−60:32:11.4	0.29	0.094	0.115	0.00	0.00	0.0	10.1	2	
317	ATHDFS_J223302.1–603213	22:33:02.18	0.33	−60:32:13.2	0.43	0.063	0.051	0.00	0.00	0.0	6.4	2	
318	ATHDFS_J223519.4–603157	22:35:19.49	0.13	−60:31:57.4	0.15	0.348	0.516	5.51	3.58	47.6	26.5	1	ATHDFS_J223518.6–603151
319	ATHDFS_J223518.6–603151	22:35:18.61	0.26	−60:31:51.3	0.25	0.147	0.145	0.00	0.00	0.0	11.2	1	ATHDFS_J223519.4–603157
320	ATHDFS_J223113.5–603147	22:31:13.53	0.17	−60:31:47.0	0.10	0.481	0.831	8.56	1.61	−72.0	31.8	1	
321	ATHDFS_J223433.9–603150	22:34:33.99	0.28	−60:31:50.0	0.59	0.055	0.044	0.00	0.00	0.0	5.8	2	
322	ATHDFS_J223449.7–603137	22:34:49.78	0.40	−60:31:37.8	0.43	0.069	0.068	0.00	0.00	0.0	6.8	2	
323	ATHDFS_J223303.1–603132	22:33:03.17	0.35	−60:31:32.8	0.47	0.052	0.035	0.00	0.00	0.0	5.2	2	
324	ATHDFS_J223254.4–603131	22:32:54.41	0.47	−60:31:31.5	0.41	0.086	0.139	6.91	3.17	64.1	9.0	2	
325	ATHDFS_J223316.0–603127	22:33:16.09	0.43	−60:31:27.6	0.67	0.052	0.049	0.00	0.00	0.0	5.3	2	
326	ATHDFS_J223548.9–603113	22:35:48.99	0.14	−60:31:13.5	0.08	0.583	1.357	10.49	4.59	−79.7	44.4	1	
327	ATHDFS_J223201.4–603118	22:32:01.42	0.38	−60:31:18.9	0.53	0.079	0.088	0.00	0.00	0.0	6.9	2	
328	ATHDFS_J223351.7–603117	22:33:51.76	0.35	−60:31:17.3	0.86	0.061	0.075	0.00	0.00	0.0	5.7	2	
329	ATHDFS_J223504.6–603109	22:35:04.63	0.33	−60:31:09.3	0.29	0.138	0.181	0.00	0.00	0.0	11.8	2	
330	ATHDFS_J223415.5–603108	22:34:15.51	0.26	−60:31:08.3	0.42	0.075	0.062	0.00	0.00	0.0	7.4	2	
331	ATHDFS_J223256.4–603058	22:32:56.42	0.39	−60:30:58.9	0.35	0.074	0.087	0.00	0.00	0.0	8.5	2	
332	ATHDFS_J223550.9–603050	22:35:50.97	0.28	−60:30:50.2	0.58	0.072	0.050	0.00	0.00	0.0	5.5	2	
333	ATHDFS_J223447.4–603050	22:34:47.48	0.60	−60:30:50.1	0.40	0.062	0.061	0.00	0.00	0.0	5.7	2	
334	ATHDFS_J223146.0–603046	22:31:46.03	0.41	−60:30:46.6	0.41	0.099	0.099	0.00	0.00	0.0	7.7	2	
335	ATHDFS_J223345.0–603041	22:33:45.06	0.18	−60:30:41.4	0.27	0.116	0.108	0.00	0.00	0.0	12.0	2	
336	ATHDFS_J223404.0–603037	22:34:04.02	0.24	−60:30:37.6	0.27	0.140	0.190	4.90	2.88	51.3	14.0	1	ATHDFS_J223405.3–603029
337	ATHDFS_J223405.3–603029	22:34:05.30	0.28	−60:30:29.2	0.27	0.116	0.132	0.00	0.00	0.0	11.8	1	ATHDFS_J223404.0–603037
338	ATHDFS_J223445.6–603032	22:34:45.67	0.59	−60:30:32.3	0.70	0.057	0.062	0.00	0.00	0.0	5.0	2	
339	ATHDFS_J223304.8–603031	22:33:04.89	0.44	−60:30:31.2	0.25	0.084	0.082	0.00	0.00	0.0	8.2	2	
340	ATHDFS_J223120.1–603025	22:31:20.18	0.52	−60:30:25.7	0.91	0.077	0.102	0.00	0.00	0.0	5.0	2	
341	ATHDFS_J223537.7–603013	22:35:37.72	0.04	−60:30:13.3	0.04	1.562	2.860	6.70	5.33	52.3	103.0	1	
342	ATHDFS_J223241.4–603025	22:32:41.42	0.30	−60:30:25.9	0.27	0.092	0.080	0.00	0.00	0.0	9.4	2	
343	ATHDFS_J223414.6–603024	22:34:14.61	0.49	−60:30:24.7	0.28	0.099	0.135	0.00	0.00	0.0	9.5	2	
344	ATHDFS_J223440.4–603017	22:34:40.40	0.18	−60:30:17.7	0.24	0.187	0.226	0.00	0.00	0.0	16.3	2	
345	ATHDFS_J223216.6–603016	22:32:16.67	0.54	−60:30:16.7	0.51	0.052	0.046	0.00	0.00	0.0	5.2	2	
346	ATHDFS_J223453.7–603008	22:34:53.72	0.25	−60:30:08.9	0.27	0.181	0.222	4.11	1.61	62.0	12.7	2	
347	ATHDFS_J223303.9–603013	22:33:03.96	0.46	−60:30:13.6	1.05	0.052	0.072	0.00	0.00	0.0	5.1	2	
348	ATHDFS_J223203.6–603007	22:32:03.67	0.16	−60:30:07.0	0.14	0.256	0.380	6.63	1.85	−63.0	25.7	1	
349	ATHDFS_J223331.1–603007	22:33:31.14	0.31	−60:30:07.9	0.40	0.094	0.107	0.00	0.00	0.0	9.0	2	
350	ATHDFS_J223430.1–602959	22:34:30.11	0.12	−60:29:59.4	0.15	0.284	0.441	5.94	3.88	35.3	27.8	1	
351	ATHDFS_J223236.5–603000	22:32:36.56	0.02	−60:30:00.6	0.03	1.300	1.507	3.71	1.33	−30.0	129.7	1	
352	ATHDFS_J223224.7–603005	22:32:24.77	0.66	−60:30:05.5	0.47	0.055	0.055	0.00	0.00	0.0	5.1	2	
353	ATHDFS_J223516.8–602959	22:35:16.84	0.36	−60:29:59.4	0.26	0.163	0.226	5.88	0.76	88.6	11.4	2	
354	ATHDFS_J223355.5–602956	22:33:55.54	0.02	−60:29:56.4	0.03	1.364	1.534	3.51	0.24	23.7	142.0	1	
355	ATHDFS_J223058.4–602952	22:30:58.48	0.84	−60:29:52.3	0.70	0.110	0.229	8.59	5.12	−67.9	5.9	2	
356	ATHDFS_J223544.3–602950	22:35:44.33	1.11	−60:29:50.7	0.94	0.097	0.105	0.00	0.00	0.0	6.1	n	
357	ATHDFS_J223530.9–602951	22:35:30.90	0.49	−60:29:51.4	0.41	0.115	0.158	5.80	1.03	68.2	8.0	2	

Table 1—Continued

ID	source	RA	σ_α	Dec	σ_δ	S_{peak}	S_{int}	θ_{maj}	θ_{min}	PA	SN_{local}	Flag	Notes
358	ATHDFS_J223534.2–602948	22:35:34.20	0.44	−60:29:48.3	0.94	0.086	0.138	7.73	2.69	4.5	5.8	2	
359	ATHDFS_J223108.1–602946	22:31:08.17	0.50	−60:29:46.5	0.31	0.138	0.185	0.00	0.00	0.0	8.7	2	
360	ATHDFS_J223410.0–602949	22:34:10.03	0.43	−60:29:49.9	0.43	0.078	0.095	0.00	0.00	0.0	7.7	2	
361	ATHDFS_J223253.7–602946	22:32:53.78	0.38	−60:29:46.7	0.52	0.045	0.034	0.00	0.00	0.0	5.1	2	
362	ATHDFS_J223316.8–602934	22:33:16.80	0.03	−60:29:34.7	0.05	0.823	1.003	4.26	1.88	6.0	76.5	1	
363	ATHDFS_J223329.1–602933	22:33:29.16	0.12	−60:29:33.4	0.22	0.203	0.261	5.36	1.30	3.5	20.3	1	
364	ATHDFS_J223513.7–602930	22:35:13.71	0.46	−60:29:30.1	0.41	0.115	0.172	6.47	2.24	62.0	8.8	2	
365	ATHDFS_J223140.6–602924	22:31:40.62	0.01	−60:29:24.7	0.01	3.689	4.962	5.39	1.89	−54.5	247.9	1	
366	ATHDFS_J223454.1–602926	22:34:54.16	0.18	−60:29:26.5	0.29	0.206	0.264	5.22	1.32	21.5	14.6	1	
367	ATHDFS_J223303.0–602927	22:33:03.00	0.34	−60:29:27.1	0.67	0.082	0.116	7.22	3.83	−1.4	8.2	1	
368	ATHDFS_J223301.8–602930	22:33:01.82	0.41	−60:29:30.2	0.72	0.071	0.119	0.00	0.00	0.0	7.1	1	ATHDFS_J223301.8–602930
369	ATHDFS_J223415.3–602925	22:34:15.33	0.16	−60:29:25.5	0.18	0.208	0.291	4.63	3.69	63.1	21.3	1	ATHDFS_J223303.0–602927
370	ATHDFS_J223149.1–602924	22:31:49.11	0.57	−60:29:24.1	0.70	0.079	0.108	0.00	0.00	0.0	5.6	2	
371	ATHDFS_J223157.5–602919	22:31:57.53	0.23	−60:29:19.2	0.28	0.142	0.151	0.00	0.00	0.0	11.6	2	
372	ATHDFS_J223447.1–602915	22:34:47.11	0.13	−60:29:15.8	0.13	0.300	0.326	0.00	0.00	0.0	24.3	1	
373	ATHDFS_J223407.4–602913	22:34:07.43	0.30	−60:29:13.9	0.35	0.098	0.109	0.00	0.00	0.0	9.8	2	
374	ATHDFS_J223317.7–602916	22:33:17.72	0.50	−60:29:16.0	0.72	0.059	0.068	0.00	0.00	0.0	5.2	2	
375	ATHDFS_J223117.4–602850	22:31:17.48	0.06	−60:28:50.1	0.04	2.356	7.756	16.93	4.28	−56.8	138.9	1	
376	ATHDFS_J223515.2–602856	22:35:15.23	0.23	−60:28:56.3	0.29	0.175	0.239	0.00	0.00	0.0	14.4	1	
377	ATHDFS_J223420.1–602901	22:34:20.14	0.83	−60:29:01.8	0.50	0.059	0.077	0.00	0.00	0.0	5.9	2	
378	ATHDFS_J223445.3–602855	22:34:45.36	0.19	−60:28:55.8	0.22	0.209	0.276	5.27	1.56	46.0	17.2	1	
379	ATHDFS_J223431.7–602859	22:34:31.76	0.53	−60:28:59.5	0.84	0.057	0.071	0.00	0.00	0.0	5.1	2	
380	ATHDFS_J223212.1–602858	22:32:12.18	0.22	−60:28:58.4	0.31	0.119	0.124	0.00	0.00	0.0	11.2	2	
381	ATHDFS_J223505.0–602853	22:35:05.00	0.22	−60:28:53.4	0.34	0.150	0.187	0.00	0.00	0.0	12.4	2	
382	ATHDFS_J223236.2–602855	22:32:36.20	0.31	−60:28:55.6	0.62	0.079	0.094	0.00	0.00	0.0	7.5	2	
383	ATHDFS_J223108.3–602851	22:31:08.34	0.67	−60:28:51.6	0.54	0.078	0.086	0.00	0.00	0.0	5.0	2	
384	ATHDFS_J223307.7–602853	22:33:07.73	0.25	−60:28:53.8	0.55	0.068	0.053	0.00	0.00	0.0	6.5	2	
385	ATHDFS_J223127.7–602849	22:31:27.71	0.70	−60:28:49.2	0.53	0.085	0.120	0.00	0.00	0.0	5.8	2	
386	ATHDFS_J223326.9–602850	22:33:26.94	0.15	−60:28:50.0	0.22	0.165	0.182	2.93	1.13	−5.7	16.3	1	
387	ATHDFS_J223330.5–602849	22:33:30.55	0.51	−60:28:49.7	0.90	0.047	0.061	0.00	0.00	0.0	5.0	2	
388	ATHDFS_J223103.5–602830	22:31:03.51	0.58	−60:28:30.7	0.64	0.116	0.190	6.82	3.63	−47.5	6.6	2	
389	ATHDFS_J223138.5–602834	22:31:38.51	0.63	−60:28:34.0	0.93	0.081	0.106	0.00	0.00	0.0	5.0	2	
390	ATHDFS_J223307.0–602827	22:33:07.07	0.11	−60:28:27.8	0.15	0.272	0.354	4.58	2.60	32.4	26.6	1	
391	ATHDFS_J223436.2–602821	22:34:36.23	0.55	−60:28:21.8	0.33	0.103	0.148	0.00	0.00	0.0	8.4	2	
392	ATHDFS_J223329.4–602811	22:33:29.40	0.36	−60:28:11.8	0.45	0.077	0.091	0.00	0.00	0.0	7.9	2	
393	ATHDFS_J223255.9–602810	22:32:55.99	0.20	−60:28:10.1	0.38	0.108	0.112	0.00	0.00	0.0	10.3	2	
394	ATHDFS_J223413.3–602808	22:34:13.30	0.51	−60:28:08.3	0.54	0.075	0.110	5.51	3.35	56.8	7.0	2	
395	ATHDFS_J223427.0–602802	22:34:27.02	0.92	−60:28:02.4	0.90	0.069	0.141	10.60	2.53	48.8	5.5	2	
396	ATHDFS_J223219.7–602802	22:32:19.73	0.61	−60:28:02.7	0.77	0.077	0.141	6.47	5.56	−1.9	6.0	2	
397	ATHDFS_J223114.1–602800	22:31:14.13	0.78	−60:28:00.3	0.57	0.109	0.153	0.00	0.00	0.0	5.9	2	
398	ATHDFS_J223133.4–602755	22:31:33.40	0.62	−60:27:55.1	1.35	0.081	0.196	11.47	4.81	11.2	5.1	2	
399	ATHDFS_J223240.7–602755	22:32:40.71	0.34	−60:27:55.3	0.38	0.112	0.139	3.77	2.56	68.0	9.2	2	
400	ATHDFS_J223438.4–602747	22:34:38.40	0.45	−60:27:47.2	0.48	0.116	0.149	0.00	0.00	0.0	8.4	2	
401	ATHDFS_J223454.2–602742	22:34:54.23	0.16	−60:27:42.5	0.17	0.262	0.370	5.84	2.11	48.6	22.4	1	
402	ATHDFS_J223443.9–602739	22:34:43.99	0.05	−60:27:39.6	0.06	0.961	1.360	5.57	2.67	46.9	69.3	1	ATHDFS_J223443.0–602734,ATHDFS_J223442.0–602729
403	ATHDFS_J223443.0–602734	22:34:43.03	0.06	−60:27:34.4	0.07	0.774	1.221	5.43	4.60	53.2	55.8	1	ATHDFS_J223443.9–602739,ATHDFS_J223442.0–602729
404	ATHDFS_J223442.0–602729	22:34:42.01	0.14	−60:27:29.7	0.14	0.442	0.883	7.11	6.07	−83.2	31.9	1	ATHDFS_J223443.9–602739,ATHDFS_J223443.0–602734
405	ATHDFS_J223136.1–602731	22:31:36.13	0.65	−60:27:31.5	0.51	0.104	0.151	6.42	1.28	−69.1	6.5	2	
406	ATHDFS_J223311.5–602725	22:33:11.53	0.32	−60:27:25.1	0.40	0.150	0.344	9.06	6.09	33.7	13.2	2	
407	ATHDFS_J223142.7–602719	22:31:42.73	0.44	−60:27:19.6	0.91	0.126	0.338	12.75	5.25	−15.8	7.9	2	
408	ATHDFS_J223153.1–602723	22:31:53.19	0.35	−60:27:23.3	0.41	0.105	0.119	0.00	0.00	0.0	8.1	2	

Table 1—Continued

ID	source	RA	σ_α	Dec	σ_δ	S_{peak}	S_{int}	θ_{maj}	θ_{min}	PA	SN_{local}	Flag	Notes
409	ATHDFS_J223148.6-602722	22:31:48.67	0.60	-60:27:22.0	0.86	0.080	0.132	6.71	4.04	24.7	5.5	2	
410	ATHDFS_J223332.7-602723	22:33:32.77	0.36	-60:27:23.5	0.52	0.074	0.087	0.00	0.00	0.0	8.0	2	
411	ATHDFS_J223241.5-602719	22:32:41.50	0.09	-60:27:19.8	0.13	0.351	0.391	0.00	0.00	0.0	28.0	1	
412	ATHDFS_J223227.6-602719	22:32:27.60	0.17	-60:27:19.0	0.27	0.218	0.306	5.64	2.84	-15.8	16.9	1	ATHDFS_J223228.4-602710
413	ATHDFS_J223228.4-602710	22:32:28.45	0.39	-60:27:10.0	0.54	0.090	0.108	0.00	0.00	0.0	7.0	1	ATHDFS_J223227.6-602719
414	ATHDFS_J223418.3-602715	22:34:18.36	0.51	-60:27:15.6	0.56	0.097	0.196	9.37	4.08	-45.6	8.8	2	
415	ATHDFS_J223244.5-602719	22:32:44.57	0.33	-60:27:19.2	0.60	0.088	0.103	0.00	0.00	0.0	7.0	2	
416	ATHDFS_J223317.1-602714	22:33:17.11	0.38	-60:27:14.1	0.73	0.079	0.122	8.19	0.86	-22.1	7.6	2	
417	ATHDFS_J223312.3-602707	22:33:12.30	0.41	-60:27:07.9	0.51	0.078	0.088	0.00	0.00	0.0	7.0	2	
418	ATHDFS_J223415.2-602701	22:34:15.26	0.35	-60:27:01.1	0.93	0.055	0.060	0.00	0.00	0.0	5.1	2	
419	ATHDFS_J223257.4-602657	22:32:57.44	0.39	-60:26:57.4	0.49	0.083	0.090	0.00	0.00	0.0	7.3	2	
420	ATHDFS_J223329.0-602657	22:33:29.08	0.72	-60:26:57.1	0.58	0.054	0.067	0.00	0.00	0.0	5.3	2	
421	ATHDFS_J223432.3-602652	22:34:32.34	0.40	-60:26:52.5	0.50	0.085	0.096	0.00	0.00	0.0	6.9	2	
422	ATHDFS_J223259.9-602654	22:32:59.93	0.33	-60:26:54.8	0.69	0.061	0.057	0.00	0.00	0.0	5.5	2	
423	ATHDFS_J223506.2-602647	22:35:06.28	0.43	-60:26:47.2	0.70	0.078	0.071	0.00	0.00	0.0	5.2	2	
424	ATHDFS_J223359.1-602642	22:33:59.14	0.16	-60:26:42.3	0.24	0.159	0.184	3.77	1.22	17.2	16.2	1	
425	ATHDFS_J223342.2-602639	22:33:42.23	0.43	-60:26:39.4	0.56	0.084	0.130	5.59	4.24	22.9	7.7	2	
426	ATHDFS_J223221.4-602629	22:32:21.49	0.01	-60:26:29.7	0.01	3.280	4.274	5.14	1.95	-29.6	280.9	1	
427	ATHDFS_J223400.9-602633	22:34:00.95	0.36	-60:26:33.6	0.34	0.087	0.097	0.00	0.00	0.0	8.8	2	
428	ATHDFS_J223212.4-602632	22:32:12.42	0.58	-60:26:32.2	0.91	0.075	0.143	8.00	4.79	-15.6	5.8	2	
429	ATHDFS_J223136.2-602627	22:31:36.23	0.46	-60:26:27.6	0.71	0.113	0.150	0.00	0.00	0.0	6.1	2	
430	ATHDFS_J223432.6-602614	22:34:32.68	0.18	-60:26:14.3	0.26	0.211	0.318	7.26	1.50	32.7	18.2	1	
431	ATHDFS_J223335.3-602615	22:33:35.35	0.16	-60:26:15.0	0.28	0.162	0.172	0.00	0.00	0.0	13.7	2	
432	ATHDFS_J223136.9-602610	22:31:36.98	0.43	-60:26:10.8	0.48	0.124	0.131	0.00	0.00	0.0	6.6	2	
433	ATHDFS_J223322.5-602607	22:33:22.57	0.66	-60:26:07.5	0.46	0.062	0.073	0.00	0.00	0.0	5.8	2	
434	ATHDFS_J223442.5-602601	22:34:42.54	0.56	-60:26:01.4	0.71	0.056	0.056	0.00	0.00	0.0	5.2	2	
435	ATHDFS_J223307.2-602556	22:33:07.25	0.17	-60:25:56.5	0.23	0.186	0.234	4.01	2.83	-3.7	16.7	1	
436	ATHDFS_J223148.3-602554	22:31:48.30	0.37	-60:25:54.0	0.49	0.132	0.210	7.86	1.93	-36.7	9.9	1	
437	ATHDFS_J223357.8-602548	22:33:57.83	0.53	-60:25:48.0	0.46	0.101	0.164	6.50	3.70	73.1	8.0	2	
438	ATHDFS_J223308.8-602540	22:33:08.86	0.56	-60:25:40.6	0.51	0.071	0.095	0.00	0.00	0.0	6.6	2	
439	ATHDFS_J223202.6-602534	22:32:02.64	0.32	-60:25:34.5	0.40	0.143	0.174	0.00	0.00	0.0	9.7	2	
440	ATHDFS_J223222.4-602532	22:32:22.49	0.23	-60:25:32.3	0.49	0.105	0.099	0.00	0.00	0.0	7.7	2	
441	ATHDFS_J223432.2-602530	22:34:32.29	0.50	-60:25:30.1	0.39	0.074	0.070	0.00	0.00	0.0	6.1	2	
442	ATHDFS_J223445.7-602523	22:34:45.70	0.63	-60:25:23.1	0.58	0.105	0.181	0.00	0.00	0.0	7.5	2	
443	ATHDFS_J223351.2-602519	22:33:51.24	0.51	-60:25:19.6	0.80	0.068	0.103	7.34	2.03	-29.2	6.2	2	
444	ATHDFS_J223141.1-602506	22:31:41.17	0.92	-60:25:06.6	1.18	0.098	0.301	14.80	5.24	-37.3	5.8	2	
445	ATHDFS_J223228.9-602507	22:32:28.94	0.29	-60:25:07.9	0.35	0.135	0.164	0.00	0.00	0.0	10.9	2	
446	ATHDFS_J223134.5-602457	22:31:34.57	0.23	-60:24:57.4	0.26	0.263	0.416	6.87	3.05	-47.4	16.4	1	
447	ATHDFS_J223306.6-602425	22:33:06.60	0.02	-60:24:25.9	0.03	1.577	1.949	5.04	0.79	-4.0	134.8	1	
448	ATHDFS_J223317.1-602427	22:33:17.16	0.12	-60:24:27.6	0.18	0.226	0.232	0.00	0.00	0.0	19.2	1	
449	ATHDFS_J223444.9-602417	22:34:44.90	0.01	-60:24:17.1	0.01	5.735	9.581	8.23	2.20	33.8	381.0	1	
450	ATHDFS_J223436.8-602426	22:34:36.87	0.64	-60:24:26.8	0.96	0.076	0.128	8.23	2.34	31.6	5.4	2	
451	ATHDFS_J223245.3-602407	22:32:45.39	0.09	-60:24:07.7	0.14	0.384	0.469	4.46	1.58	-20.1	29.1	1	
452	ATHDFS_J223343.4-602348	22:33:43.43	0.68	-60:23:48.8	1.26	0.067	0.111	0.00	0.00	0.0	5.2	2	
453	ATHDFS_J223410.2-602324	22:34:10.27	0.08	-60:23:24.2	0.15	0.455	0.582	0.00	0.00	0.0	30.4	1	
454	ATHDFS_J223146.3-602313	22:31:46.37	0.34	-60:23:13.7	0.50	0.194	0.465	10.37	5.60	-27.4	11.9	2	
455	ATHDFS_J223331.6-602307	22:33:31.68	0.04	-60:23:07.7	0.07	0.835	1.009	0.00	0.00	0.0	63.8	1	
456	ATHDFS_J223343.7-602307	22:33:43.76	0.41	-60:23:07.3	0.74	0.092	0.127	6.39	1.13	20.5	6.4	2	
457	ATHDFS_J223358.9-602258	22:33:58.90	0.38	-60:22:58.9	0.72	0.080	0.082	0.00	0.00	0.0	5.5	2	
458	ATHDFS_J223300.5-602225	22:33:00.57	0.39	-60:22:25.8	0.76	0.073	0.073	0.00	0.00	0.0	5.5	2	
459	ATHDFS_J223154.6-602211	22:31:54.67	0.54	-60:22:11.7	0.69	0.103	0.123	0.00	0.00	0.0	5.7	2	

Table 1—Continued

ID	source	RA	σ_α	Dec	σ_δ	S_{peak}	S_{int}	θ_{maj}	θ_{min}	PA	SN_{local}	Flag	Notes
460	ATHDFS_J223353.6–602136	22:33:53.69	0.53	–60:21:36.3	0.69	0.086	0.113	0.00	0.00	0.0	5.8	2	
461	ATHDFS_J223341.1–602054	22:33:41.11	0.21	–60:20:54.1	0.48	0.122	0.125	0.00	0.00	0.0	8.9	2	
462	ATHDFS_J223359.4–602047	22:33:59.46	0.43	–60:20:47.8	0.79	0.102	0.152	7.41	1.14	23.3	6.5	2	
463	ATHDFS_J223431.4–602041	22:34:31.48	0.29	–60:20:41.3	0.32	0.254	0.595	7.80	7.57	48.1	15.3	1	
464	ATHDFS_J223356.6–601949	22:33:56.68	0.20	–60:19:49.9	0.32	0.259	0.419	7.59	2.71	25.7	16.0	1	
465	ATHDFS_J223316.0–601939	22:33:16.02	0.40	–60:19:39.0	0.72	0.159	0.327	9.03	4.86	7.9	8.1	2	
466	ATHDFS_J223334.5–601928	22:33:34.53	0.57	–60:19:28.7	0.81	0.115	0.206	8.44	3.21	32.8	6.4	2	

Table 2. The ATHDFS 1.4 GHz source counts.

Range in S (mJy)	$\langle S \rangle$ (mJy)	N	N_{eff}	$(dN/dS)/S^{-2.5}$ ($\text{Jy}^{1.5}\text{sr}^{-1}$)
0.050 – 0.064	0.059	28	226.1	4.02 ± 0.76
0.064 – 0.082	0.073	53	149.8	3.51 ± 0.48
0.082 – 0.106	0.094	70	143.0	4.90 ± 0.59
0.106 – 0.136	0.119	54	87.06	4.25 ± 0.58
0.136 – 0.174	0.154	52	79.85	5.73 ± 0.79
0.174 – 0.224	0.197	43	59.43	6.15 ± 0.94
0.224 – 0.287	0.253	26	33.49	5.08 ± 1.00
0.287 – 0.368	0.328	24	29.18	6.58 ± 1.34
0.368 – 0.473	0.417	22	25.18	8.06 ± 1.72
0.473 – 0.607	0.541	14	15.10	7.22 ± 1.93
0.607 – 0.779	0.667	10	10.75	6.76 ± 2.14
0.779 – 1.000	0.905	7	7.56	7.93 ± 3.00